6-1-2018

Earth-abundant nanostructured catalysts for solar fuel production at room temperature

Ahmed Khalifa Said

THE AMERICAN UNIVERSITY IN CAIRO

Nanotechnology Program

Earth-Abundant Nanostructured Catalysts for Solar Fuel Production At Room Temperature

A Thesis Submitted to

The Nanotechnology Program

in partial fulfillment of the requirements for
the degree of Master of Science

by Ahmed Mohamed Khalifa

(under the supervision of Dr. Nageh Allam)

May/2018

The thesis of Ahmed Mohamed Khalifa Said was reviewed and approved*by the following:

Nageh K. Allam
Associate Professor and Graduate Director
Physics Department
Director, Energy of Materials Laboratory (EML)
The American University in Cairo
Thesis Advisor
Chair of Committee

Ehab Noby
Assistant Professor
Chemistry Department
American University in Cairo
Internal Examiner

Rehab K. Ammar
Associate Professor
Chemistry Department
Beni-Suef University
External Examiner

Mohamed Al-Fiki
Assistant Professor
Physics Department
American University in Cairo
Moderator

*Signatures are on file in the Graduate School.

Abstract

Improving the performance of solar energy harvesting martials is a challenge facing the renewable energy industry. Over the past few decades, metal oxides have been extensively explored as photoelectrodes for solar-driven production of fuel due to their exceptional stability, semiconducting properties, abundance, and low cost. However, most metal oxides have absorption activity that is limited to the ultraviolet spectral region because of their wide band gap (> 3.0 eV). This is inconvenient because the ultraviolet spectral region contains only 3-5% of all incident solar energy. The current semiconductor technologies resort to either (i) doping as a means of narrowing the band-gap and enhancing light absorption, or (ii) decoration with metals to enhance charge separation. In the first part of the thesis, the synthesis of highly ordered titanium oxynitride nanotube arrays sensitized with Ag nanoparticles (Ag/TiON) was studied for the first time. Ag/TiON proved to be an attractive class of materials for visible-light-driven water splitting. The nanostructure topology of TiO_2, TiON and Ag/TiON was investigated using FESEM and TEM. The X-ray photoelectron spectroscopy (XPS) and the energy dispersive X-ray spectroscopy (EDS) analyses confirm the formation of the oxynitride structure. Upon their use to split water photoelectrochemically under AM 1.5 G illumination (100 mW/cm^2, 0.1 M KOH), the titanium oxynitride nanotube array films showed significant increase in the photocurrent (6 mA/cm^2) compared to the TiO_2 nanotubes counterpart (0.15 mA/cm^2). Moreover, decorating the TiON nanotubes with Ag nanoparticles (13 ±2 nm in size) resulted in exceptionally high photocurrent reaching 14 mA/cm^2 at 1.2 V_{NHE}. This enhancement in the photocurrent is related to the synergistic effects of Ag decoration, nitrogen doping, and the unique structural properties of the fabricated nanotube arrays. In the second part of the thesis, the effect of Ni alloying with Cu on the electrochemical reduction of CO_2 was studied. The GAXRD analysis confirmed the formation of mixed Cu-Ni catalysts. Linear sweep scans showed the $Cu_{70}Ni_{30}$ to have the lowest overpotential (-0.5V_{NHE}) and highest cathodic current (-1.8mA/cm^2). Chronoamperometry measurements, at -0.5 V_{NHE} in CO_2-saturated 0.1M KOH, confirmed similar pattern when no limiting current was observed for the electrochemical reduction of CO_2. This volcano effect of exceptionally high current and low overpotential was unique for 30% Ni and was attributed to CO_2 adsorption and superior charge transfer kinetics.

Table of Contents

List of Figures

List of Tables

Acknowledgement

I would like to start by thanking everyone who helped me in this amazing journey of science and discipline. Special thanks to Dr Nageh for his endless support and motivation. Dr. Nageh always challenged me and helped me push my limits. I count myself very lucky to have crossed paths with him so that I was able to learn fundamental science and many research techniques during my master. His help is always appreciated and never forgotten.

I would like to thank my professors at AUC, especially Dr. Ehab Noby for his constant guidance and support, both professionally and personally. I would also like to thank Dr. Adham Ramadan for outstanding role, initially as an instructor and then as Dean of Graduate studies. He helped open many doors for me and for that I am forever grateful.

I would like to thank the members of my thesis committee, for their gracious participation and for their constructive criticism. I would like to thank everyone at EML and YSTRC for their help and support in completing my research work.

Finally, I owe special gratitude to my parents and my sisters (Dina and Youmna) and my school teachers and my friends for their continuous and unconditional help and support.

Chapter 1: Introduction

1.1 The Energy Challenge

It is not news that the world's oil and gas prices are continuously rising due to their imminent exhaustion but more importantly, their demand is also increasing with the rise in population and the rise in energy demanding technologies. According to the world population count reported by the United nations, the world witnessed its greatest population burst in history from about 1.6 billion in 1900 to about 6 billion in 2000. Additionally, the industrial revolution of the 18th and 19th century relied on coal fuel energy; meanwhile the 20th century shifted to liquid fuel and natural gas. In 2009, the Association for the Study of Peak Oil & Gas (ASPO) projected that the oil and gas reserves would run out in 35-37 years. The forecast continued to state that by 2115 all three major fossil fuels will be depleted. Therefore, fossil fuel reserves are running out and we need to find alternative methods for fuel generation [1, 2].

Other unforeseen circumstances to our dependence on fossil fuels is its direct contribution to the greenhouse effect. Where 70% of the greenhouse effect results from CO_2 gas, the main byproduct of burning fossil fuels. Trapped CO_2 gas helps store more of the sun's heat energy leading to an increase in the earth's average temperature and the melting of the polar icecaps, this in turn leads to an increase in sea level. CO_2 emissions in the Arab world are also on the rise. Figure 1.1 summarizes CO_2 emissions from the Arab world. With Saudi Arabia being the highest producer of oil and gas, Egypt is the second most emitter of CO_2. Therefore, research initiatives in Egypt have been directed towards alternative clean energy. Due to this rise in CO_2 levels, the US increased vegetative landscapes to lower CO_2 through plant photosynthesis. Similar initiatives in the Arab world will hopefully follow [3, 4].

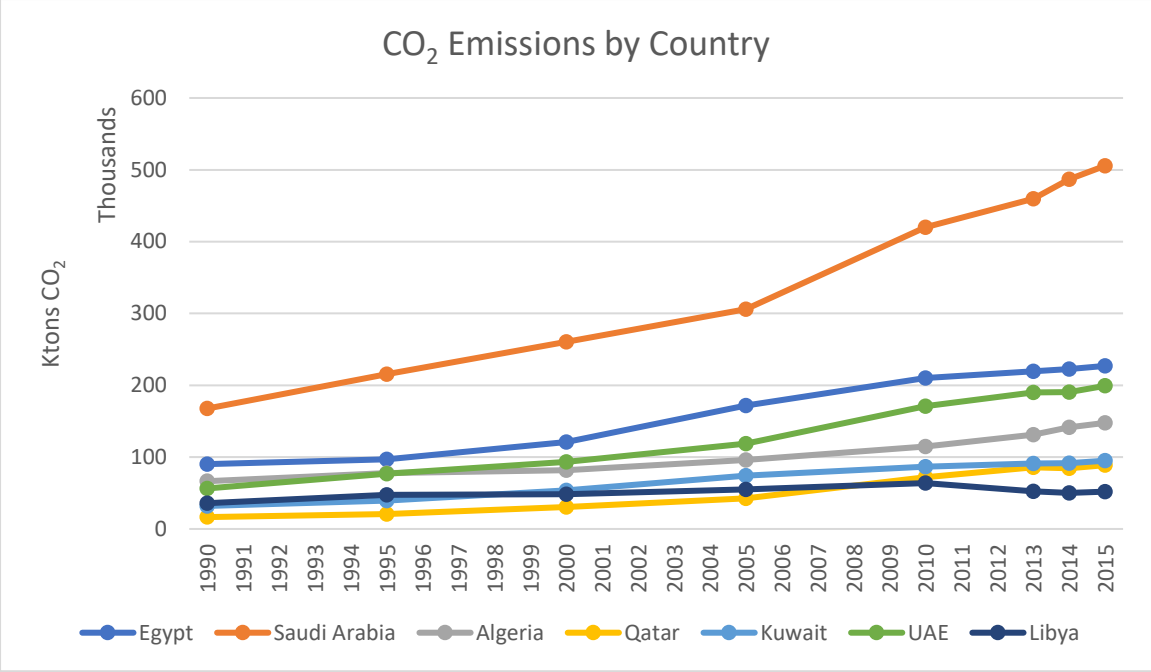

Figure 1.1 CO_2 emissions of industrial countries in the Arab world from year 1995 to 2015 [4].

1.2 Fuels for Energy

The world first started reviewing this energy crisis when Nobel prize winner, Rick Smalley studied renewable energy sources as alternatives to fossil fuels back in 1992. It was studied that the world needs to find new sources of energy that are not coal, petroleum or natural gas. The new source needs to be clean and renewable such as solar, geothermal or wind energy. This new renewable source needs to be usable, storable, clean, high in energy density and be able to provide the projected energy demand of the 28 TWy for year 2050. Therefore, a switch from traditional energy sources must be made [1]. Current energy sources and energy projections for 2050 are summarized in Figure 1.2. Figure 1.3 shows how our dependence on our existing energy technologies should change [5].

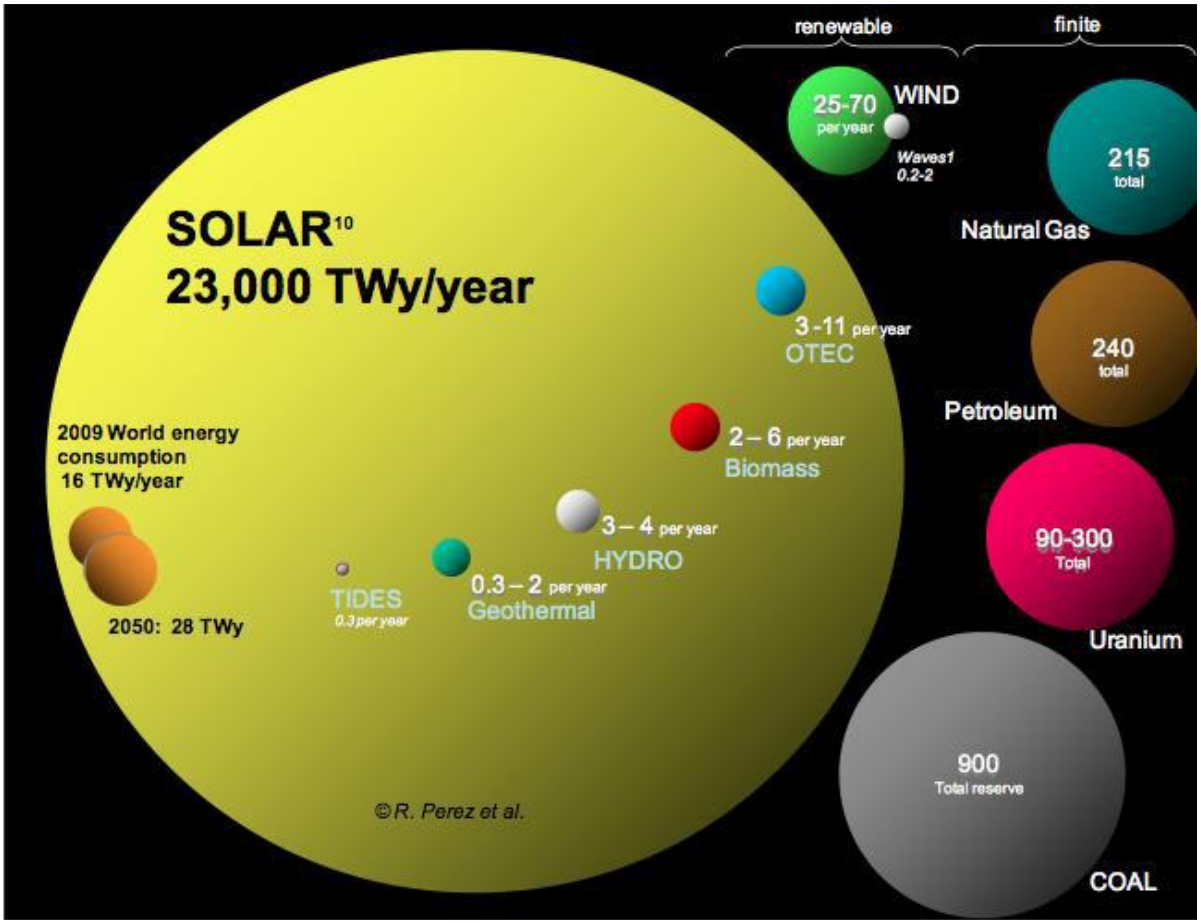

Figure 1.2 Summary of traditional and renewable energy sources [5]

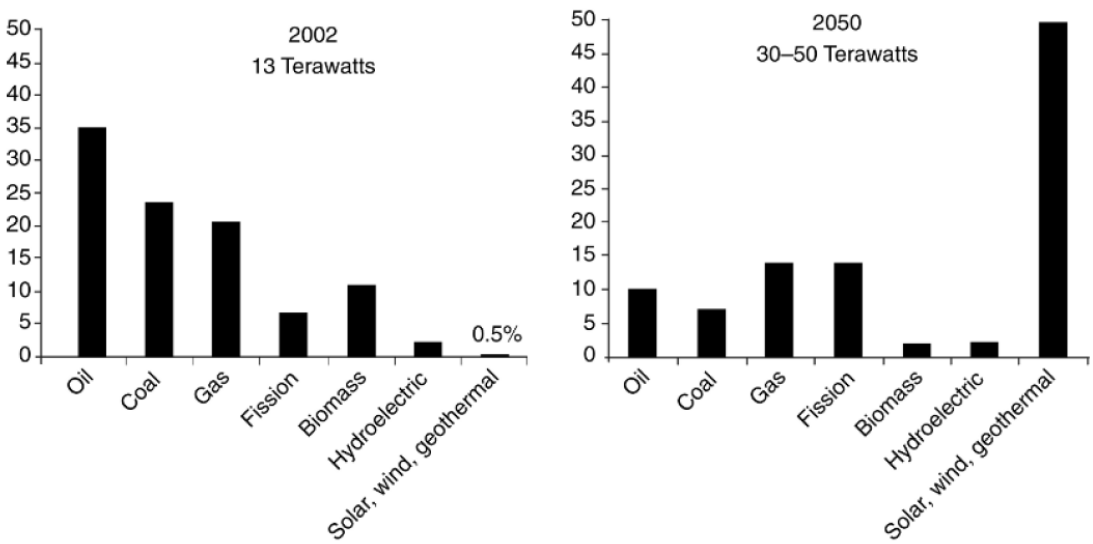

Figure 1.3 The world's dependence on energy sources and projections for 2050 [5].

1.2.1 Hydrogen

Hydrogen is important for many applications such as power generation, domestic and industrial uses, vehicles, navigation and space. More detail about these six main fields is illustrated in Figure 1.4 [6].

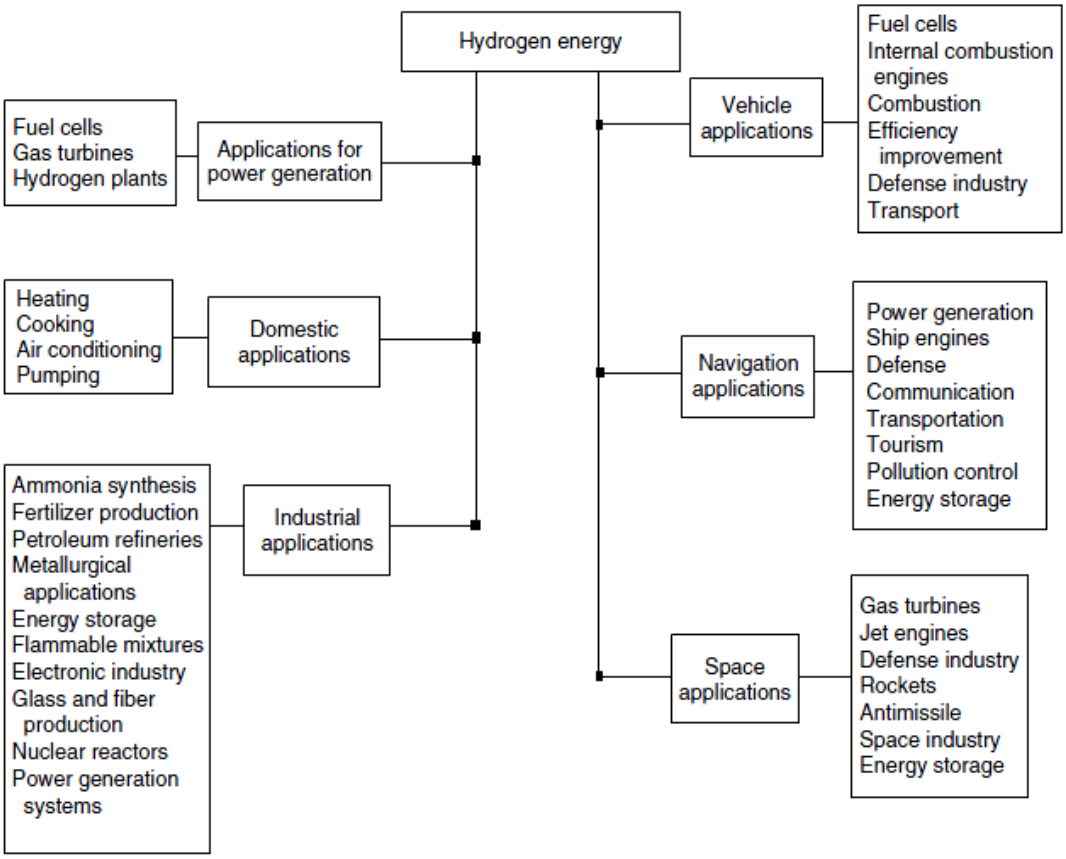

Figure 1.4 Importance of Hydrogen in the economy [6]

Hydrogen gas is a simple molecule composed of two hydrogen atoms. Hydrogen is not a primary source of energy like electricity. However, it can be used as an energy carrier. This is due to it having the highest unit energy per mass [lower heating value (LHV) and higher heating value (HHV)] of all the fuels as compared in Table 1.1 [1]. Hydrogen can be easily transported as a gas, liquid or metal hydride. This makes hydrogen particularly attractive for

the transportation industry as it can be utilized by fuel cells to generate electricity [7]. The current technologies used to produce hydrogen all rely on non-renewable sources of energy and may lead to carbon dioxide gas production. Carbon Dioxide is the main contributor to the greenhouse effect and we need to find efficient methods to reduce it back to usable fuel. Production of Hydrogen from water and the reduction of carbon dioxide is promising and efficient, only when using clean renewable solar energy, for example wind and tidal energy[8,9].

Table 1.1 A comparison of common fuels and their properties [1].

Fuel	LHV (MJ/kg)	HHV (MJ/kg)	Stoichiometric Air/Fuel Ratio (kg)	Combustible Range (%)	Flame Temperature (°C)	Min. Ignition Energy (MJ)	AutoIgnition Temperature (°C)
Methane	50.0	55.5	17.2	5–15	1914	0.30	540-630
Propane	45.6	50.3	15.6	2.1–9.5	1925	0.30	450
Octane	47.9	15.1	0.31	0.95-6.0	1980	0.26	415
Methanol	18.0	22.7	6.5	6.7-36.0	1870	0.14	460
Hydrogen	119.9	141.6	34.3	4.0-75.0	2207	0.017	585
Gasoline	44.5	47.3	14.6	1.3-7.1	2307	0.29	260-460
Diesel	42.5	44.8	14.5	0.6-5.5	2327		180-320

1.2.2 Carbon dioxide

Carbon dioxide (O=C=O) is a molecule present in the earth's atmosphere at 0.039% and serves mainly as a source of carbon for plant photosynthesis. It is a colorless odorless gas that is constantly rising in our earth's atmosphere due to the burning of fossil fuels from non-renewable sources of energy like for example, coal and petrol. Current global CO_2 emissions are approximately 37 billion tons and is estimated to reach over 50 billion tons in the next twenty years [10]. CO_2 is the main contributor to global warming and the earth has seen a rise in temperature of about 0.6K in the last century. Reducing current Carbon dioxide levels may be addressed using systems that burn fossil fuels more efficiently; using carbon free sources; or using post emission carbon capture technologies [11]. Other approaches include carbon sequestration, carbon dioxide absorption into chemical solvents and solid materials.

1.3 Solar-driven fuel production

When we think about solar energy we need to understand that while the sun can provide direct energy e.g. photovoltaics and thermal energy absorbers. Its energy may also be converted into chemical fuels.

1.3.1 Hydrogen

Water is the most abundant molecule on earth. It contains two atoms of hydrogen and one atom of oxygen. The splitting of water has been vastly sought for more than 200 years as a means of hydrogen production. Electrolysis of water with an energy of 1.229 eV (STP) breaks away the tightly bound hydrogen in water, liberating H_2 gas. The reaction below describes the energy transfer:

$$H_2O_{(l)} + \text{electrical energy} \rightarrow H_{2(g)} + \tfrac{1}{2}O_{2(g)} \qquad 1.1$$

Since the sun can not directly split water molecules into oxygen and hydrogen, a light absorbing material (such as chromophore, semiconductors or dye) must be used to harvest the suns energy and form electron/hole pairs. In 1972, Honda and Fujishima were the first to use TiO_2 as anode and Pt as cathode in aqueous electrolyte. This was the first time a photoelectrochemical (PEC) cell setup was designed to split water [12]. In this setup (Figure 1.5) oxygen was formed at the TiO_2 anode and hydrogen was formed at the Pt cathode. In comparison, TiO_2 showed better stability in water than silicon (Si) and gallium arsenide (GaAs), but suffers poor efficiency of about 0.1%. this restriction in performance is now understood to be a limitation in the semiconductor material and in the mechanism of the water splitting which will be discussed in Chapter 2.

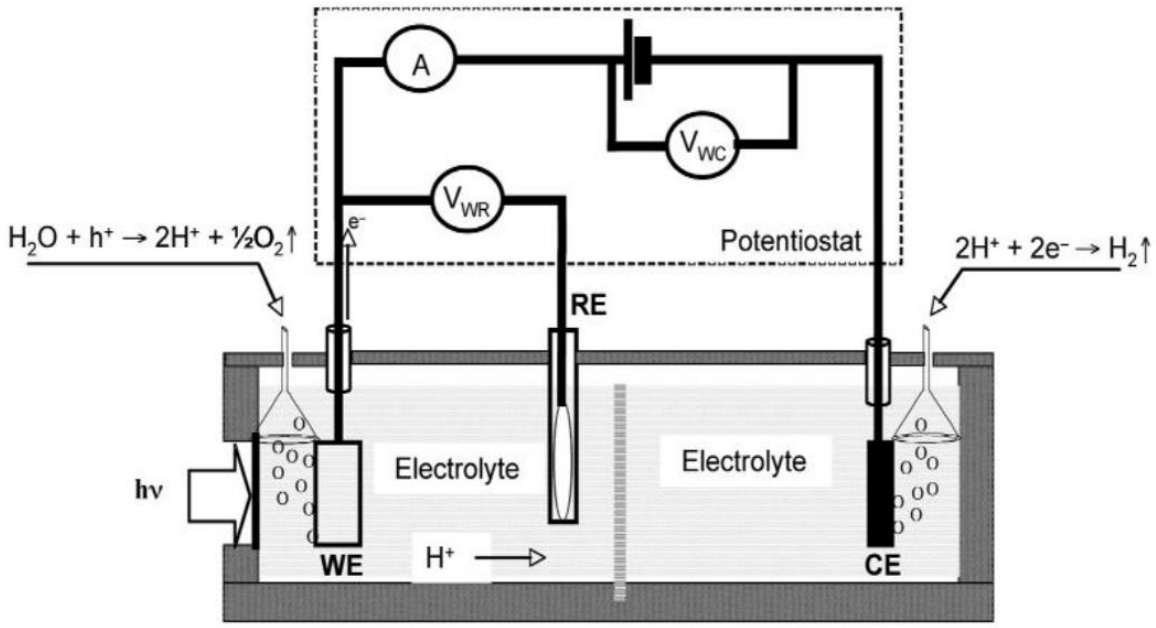

Figure 1.5 PEC three electrode setup

Despite it's low efficacy the research of Honda and Fujishima has opened the doors to many future investigations of semiconductors and their properties in water splitting. This thesis is an attempt to explore these properties.

1.3.2 Carbon dioxide

Carbon dioxide is the oxidized byproduct of fossil fuel combustion and the most stable form of this gas. The only possible way to convert and recycle this product is to chemically reduce it. There are many attempts to reduce this gas into usable fuel [13]. Like the splitting of water, the reduction of carbon dioxide to hydrocarbons is a thermodynamically uphill process (ΔG° = -394.359 kJ/mol), requiring many steps. The best case would be a setup that allows for the splitting of water to liberate hydrogen and the use of this hydrogen for carbon dioxide reduction (as shown in Figure 1.6). This is only economically feasible if the input of energy is none other than solar energy, mimicking natural photosynthesis. All other sources of CO_2 reduction are economically unfeasible.

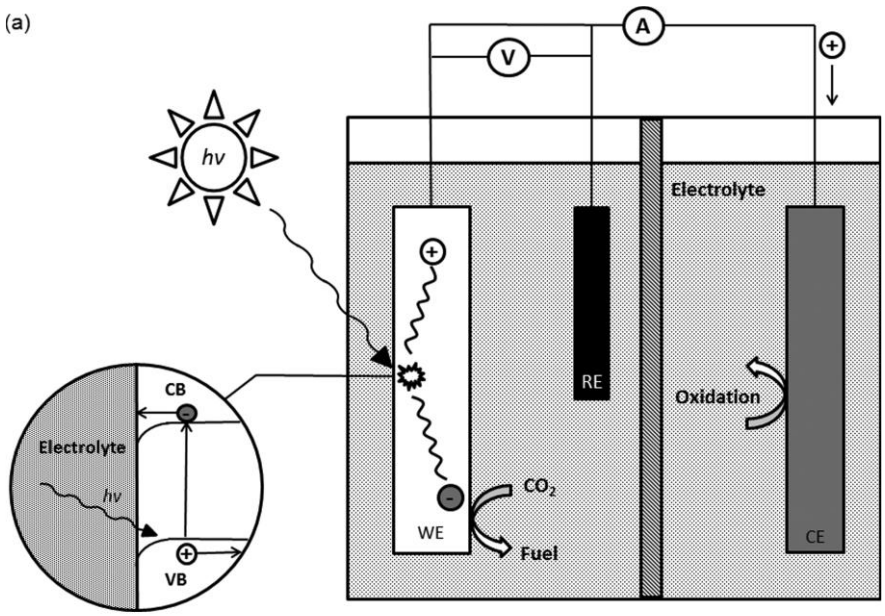

Figure 1.6 Photoelectrocatalytic CO_2 reduction setup [14]

However, the reduction reaction of CO_2 isn't straight forward. A multitude of probable reactions take place and the formed products may undergo further reduction (Figure 1.7).

Therefore, understanding the reduction of CO_2 and tuning the yield selectivity is an unclear and relatively new and challenging field of research.

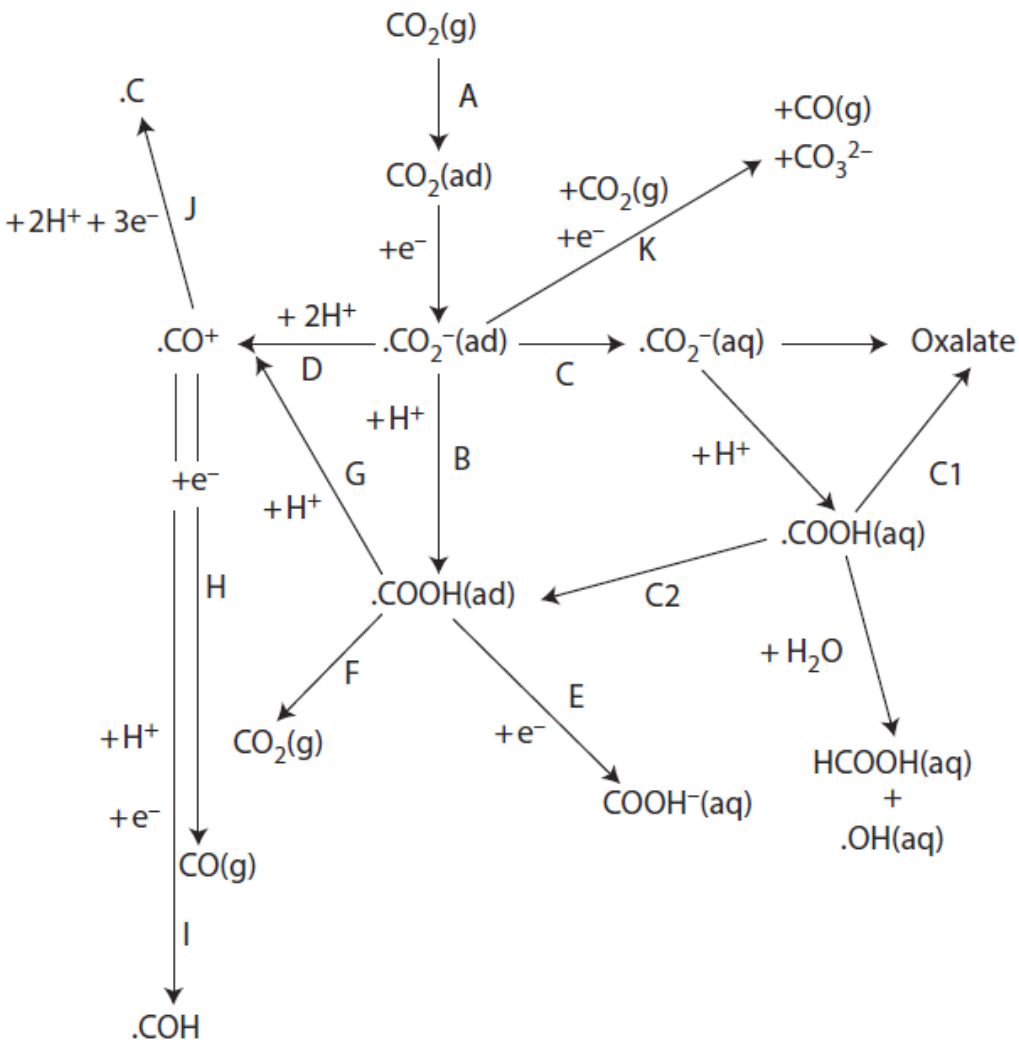

Figure 1.7 Proposed reaction pathways for the CO_2 reduction in aqueous or gaseous systems [15].

Chapter 2: Scientific Background & Literature

This chapter presents literature pertaining to scientific background and the fabrication and modifications made to titanium dioxide. This chapter pertains to the experimental work and discussions covered in this thesis. The use of titanium dioxide semiconductors in the solar water splitting and photoelectrocatalytic carbon dioxide reduction will be discussed. TiO_2 is a wide band-gap material and is therefore a non-conductive metal at STP. TiO_2 exists in three crystal configurations; Rutile, Anatase and Brookite; having band-gaps of 3 eV, 3.2 eV and 3.11 eV, respectively. These three configurations contain both covalent and ionic bonds between the Ti and O atoms. In Figure 2.1, each blue octagon comprises of one Ti and six O atoms [16, 17]. Therefore, each Ti atom has six bonds with O and each O has three bonds with Ti atoms.

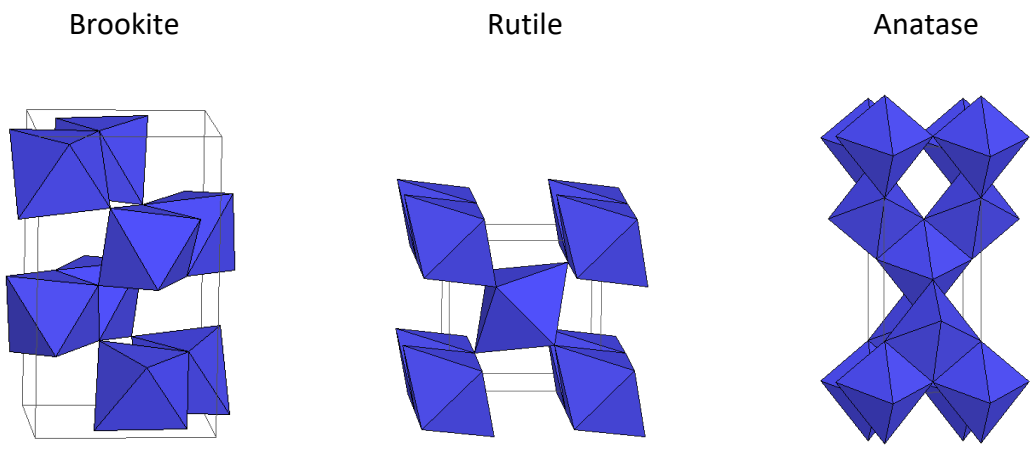

Figure 2.1 TiO_2 crystal structures: Rutile and Anatase (tetragonal) and Brookite (orthorhombic)[17]

Nanotechnology is the science of studying and manipulating molecules at the nanoscale (1-100nm). The purpose is to fabricate novel devices with improvement in properties, over the bulk materials. Through structural modification of the surface, the surface to volume ratio increases and increases the materials' sensitivity to physical, chemical or biological reactions. Therefore, many structural devices such as nanoparticles, nanowires and nanotubes are

fabricated on the nanoscale for biological and chemical applications. Similarly, the photocatalytic activity of TiO_2 can be improved by nanostructures such as nanotubes.

2.1 Heterogenous catalysis

Palmisano and Sclafani defined heterogenous photocatalysis as "a catalytic process during which one or more reaction steps occur by means of electron–hole pairs photo generated on the surface of semiconducting materials illuminated by light of suitable energy." [18]. This differs from thermal catalyzed reactions by having various product selectivity.

2.1.1 Principles of photocatalysis

Characteristic of each semiconductor is its band gap, which is defined as the energy difference (ΔE_g) between the valence band (VB) and the conduction band (CB). VB is the value of the highest electron occupied molecular orbital, whereas the CB is the value of the lowest electron unoccupied molecular orbital. When a semiconductor is illuminated with photons of energy equal to or greater than the band gap, electron/hole pairs are generated, as depicted in Figure 2.2 [19]. When these electron/hole pairs reach the surface, they react with adsorbed species to induce favorable redox reactions. Thermodynamically, holes will oxidize adsorbates when the VB has a more positive redox potential and the CB will reduce an adsorbate when its redox potential is more negative. The electron/hole pair will recombine in the absence of a species to interact with, after the termination of light. An example of oxidation is the liberation of O_2 and an example of reduction is the liberation of H_2, from H_2O. in the presence of CO_2, the photocathode may also be used to reduce CO_2 to hydrocarbons such as HCOOH, HCOH, CH_3OH and CH_4.

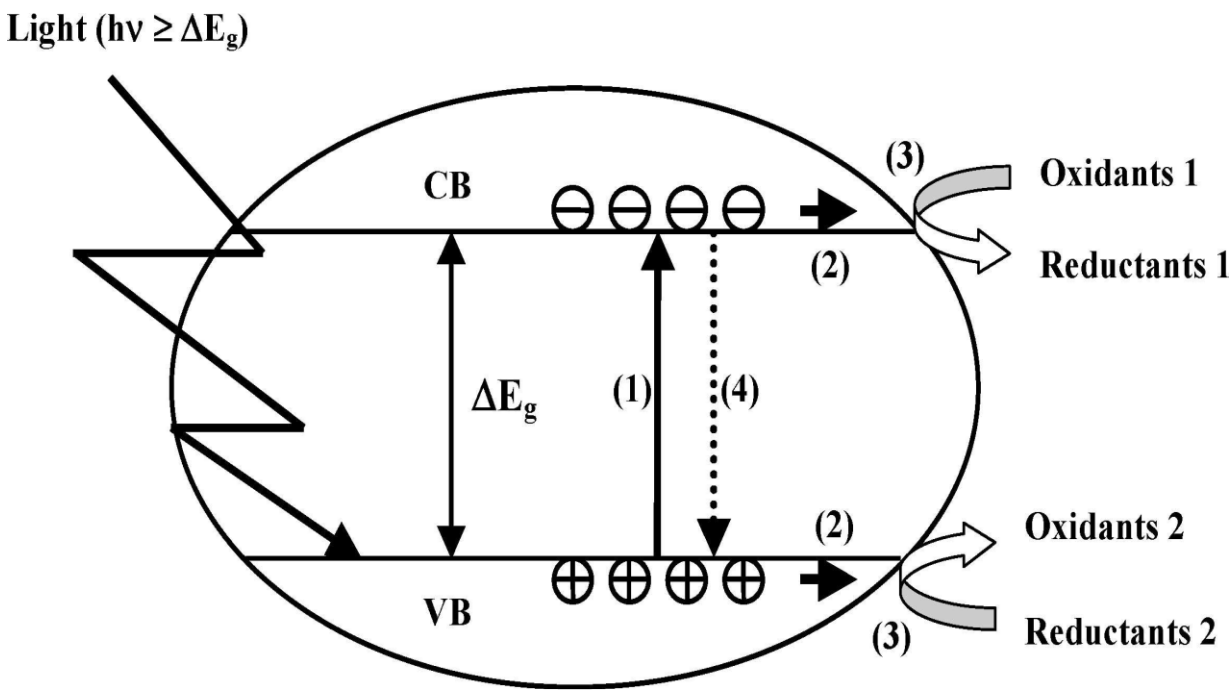

Figure 2.2 Schematic representation of the generation of electron/hole pairs upon illuminating a semiconductor. (1) Light generated electron/hole pair (2) electrons and holes move to the surface of the material (3) electrons reduce and holes oxidize adsorbed species (4) unused electron/hole pairs recombine [19]

Other factors that influence a photocatalytic reaction are [20]:

- Temperature and concentration of the reactants affects the reaction kinetics;
- pH of the supporting electrolyte
- an oversupply of photons increases recombination

To improve the light capturing capabilities of semiconductors, other components may be added to improve the overall efficiency and adapt each system to its applications. Most semiconductors studied are wide band-gap metal oxide semiconductors that absorb in the UV region of the light spectrum. Sensitizing these systems with metals and light absorbing dyes extends their light sensitivity to the visible region of the light spectrum, as shown in Figure 2.3. A dye is incorporated to absorb visible light (λ 450-700nm) then injects the electron in the semiconductor. S^0 = ground state, S^1 = excited state and S^+ = one electron oxidized state

of the sensitizer. Electrons then transfer to the metal surface where H_2 evolution is then catalyzed from an aqueous solution [21].

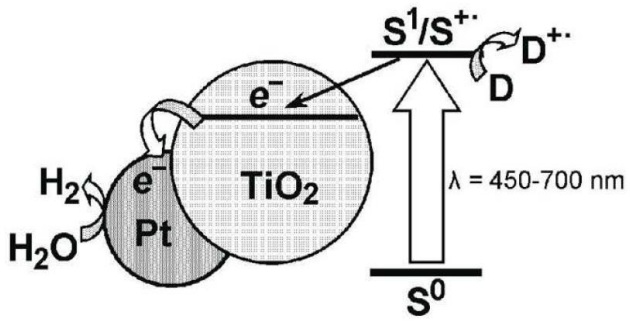

Figure 2.3 Schematic of a metal-semiconductor dye sensitized system [22]

Other binary systems combine a wide band-gap with a narrow band-gap semiconductor. Visible light is absorbed by the narrow band-gap semiconductor and generated electrons are then injected into the wide band-gap semiconductor, as depicted in Figure 2.4. This may help in electron hole separation where the hole interacts with the electron donor (D) [22].

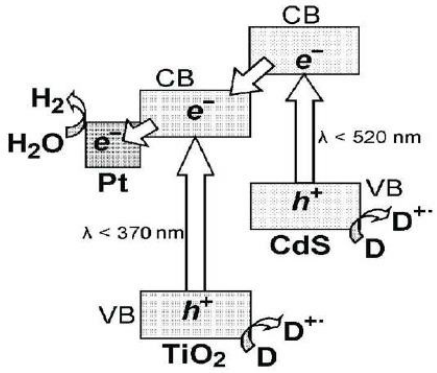

Figure 2.4 Schematic of a binary semiconductor system of TiO_2/CdS and the evolution of Hydrogen upon visible light absorption [22].

The third system involves doping of the semiconductor with transition metals cations to introduce new states is the forbidden region of the band-gap. These new states allow visible light to excite electrons into the CB as depicted in Figure 2.5.

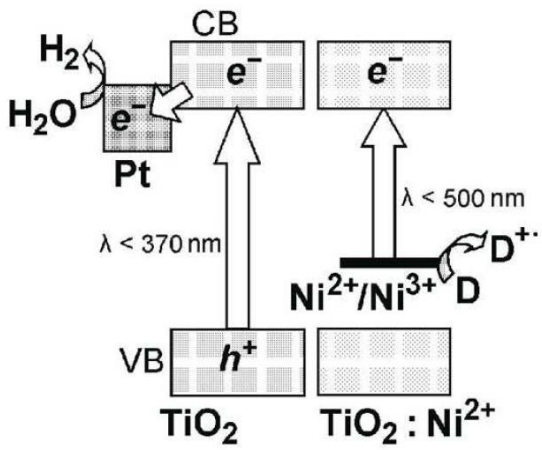

Figure 2.5 Schematic of transition metal (Ni) doping to tune absorption from λ < 370nm to λ < 500nm [22].

Another approach to narrowing the band-gap of semiconductors is the substitution of some oxygen of the metal oxide structure with elements such as nitrogen, sulfur or carbon amongst others. This is particularly effective in band-gap narrowing because the p orbitals of the substitution are located right above the p orbitals of the oxygen in the VB, as depicted in Figure 2.6.

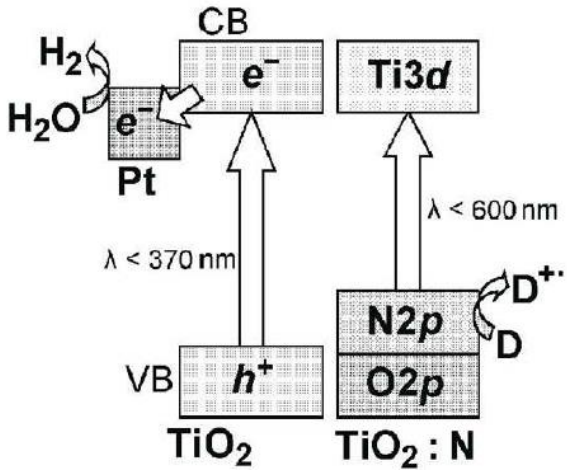

Figure 2.6 Schematic of band-gap narrowing though anion substitution [22].

2.1.2 Thermodynamics of water splitting

For water splitting, the change in Gibb's free energy is positive (ΔG = 238 kJ mol−1). Therefore, at standard temperature and pressure the splitting of water is not a spontaneous process and requires the input of energy or external bias according to the Nernst equation.

$$H_2O_{(l/g)} + electrical\ energy \rightarrow H_{2(g)} + \tfrac{1}{2}O_{2(g)},\ \Delta G = n\,F\,V_{rev} \qquad 2\text{-}1$$

In the above equation, n is the number of electrons involved in the net reaction; F is Faraday's constant. V_{rev} is the input of volts needed. While V_{rev} is theoretically calculated at 1.229 V_{NHE}, a bias of about 1.6V is required to overcome other resistances in the system. The objective in such systems is to optimize the materials in the best way to minimize this needed external bias as much as possible. Photoelectrochemical systems that incorporate a semiconductor as anode and a metal as cathode, are immersed in aqueous electrolyte and illuminated with a light source. Once connected, the system undergoes an equilibration of electrostatics across the solid-liquid interfaces. This equilibration process is given by the Nernst expression:

$$E_{redox} = E^{\circ}_{redox} + \frac{RT}{nF} + \ln\left(\frac{C_{ox}}{C_{red}}\right) \qquad 2\text{-}2$$

Where, E_{redox} is the half-cell reduction potential at T the temperature of operation in kelvin; E°_{redox} is the standard half-cell reduction potential; R is the universal gas constant; n is the number of electrons swapped in the reaction; F is Faraday constant; C_{ox} and C_{red} are the physical concentrations of the oxidized and reduced species of the redox couple, respectively. This equilibration is achieved by the transfer of charge between the interfaces resulting in band bending within the semiconductor phase. Before and after connection illustrations are depicted in Figure 2.7 (a) n-type (b) p-type semiconductors. As charge transfers, band bending continues until Fermi Level of the system = E_{redox}. This band bending results in a region at

the interface know and the depletion layer, because it is depleted of electrons. This absence of electrons creates a region of positive charge within the semiconductor at the interface. This positive charge is counteracted by negative ions from the electrolyte solution that attach on to the semiconductor surface forming the Helmholtz layer

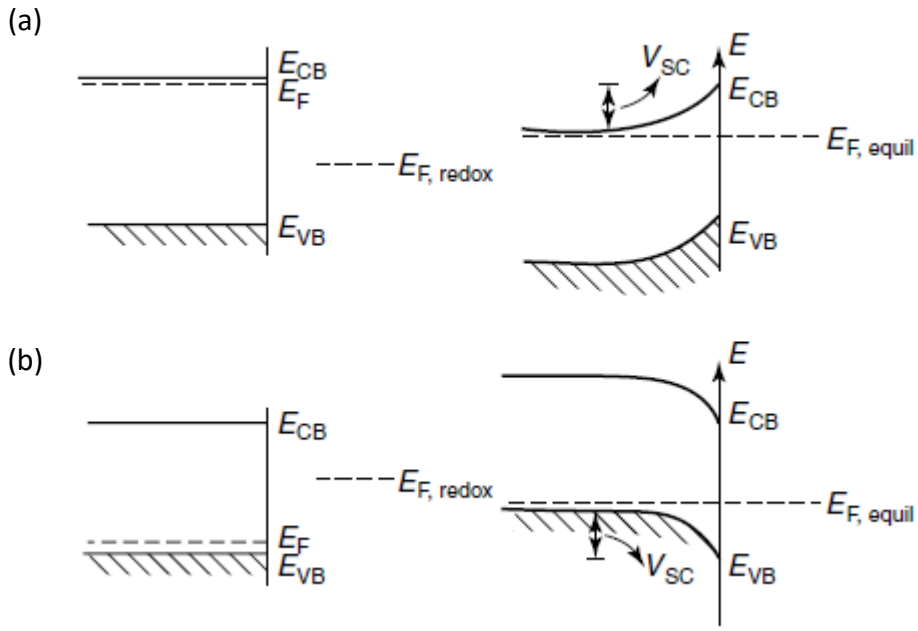

Figure 2.7 The semicondictor electrolyte interface before & after connection for (a) n-type and (b) p-type semiconductors[23]

At illumination, flat bending is reduced due to the generation of electrons, and the electric field of the depletion layer at the interface helps in separating the electrons that migrate to the surface from the holes that move to the bulk. It is clear to see now that the forward and reverse currents in the connected system are at balance and there is no net current flow at equilibration. This remains true if this semiconductor-liquid interface is not disturbed by an external bias. As shown in Figure 2.8(a), the fermi level of an n-type semiconductor is more positive that the redox potential of H^+/H_2, therefore the electrons of the semiconductor don not have enough energy to reduce the H_2 in the solution and the water splitting reaction cannot proceed without an external anodic bias, as shown in Figure 2.8(b). An external anodic

bias shifts the fermi level of the cathode more negative allowing the reduction of H_2 and water splitting now proceeds under illumination.

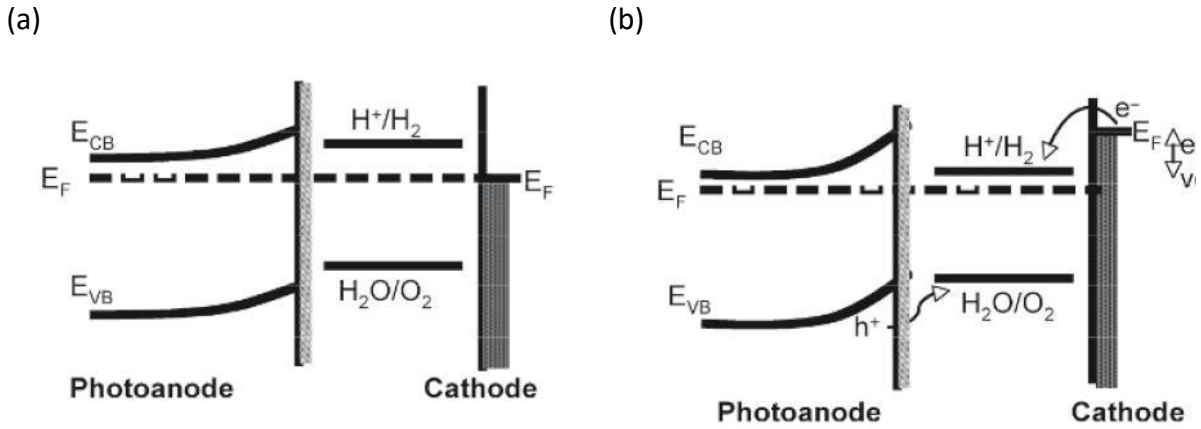

Figure 2.8 A connected n-type semiconductor (a) under illumination and (b) under illumination with anodic current [6].

Therefore, as explained above, an external bias may be needed in such n-type semiconductor systems to drive electrochemical processes. These systems may be used to drive oxidation and reduction processes such as water splitting and carbon dioxide reduction, with an anodic and cathodic bias respectively. Figure 2.9 shows the effect of positive and negative bias on an n-type semiconductor and how it relates to the E_{redox} of the system.

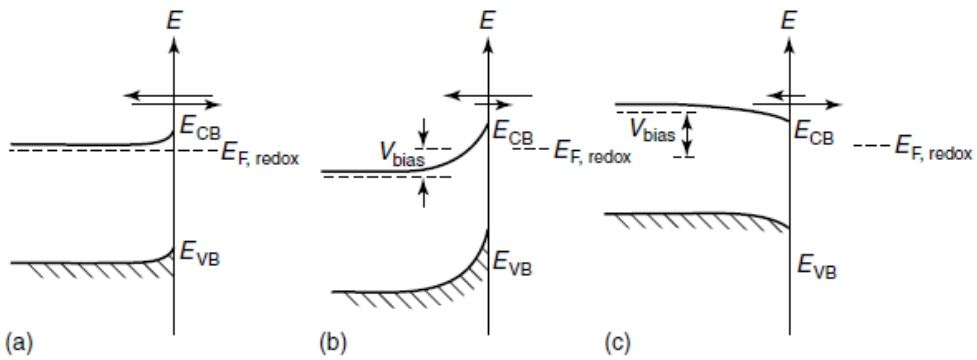

Figure 2.9 Electrolyte interface for n-type semiconductor under (a) no bias (b) anodic bias and (c) cathodic bias; the arrows indicate the size and magnitude of the observed current [23].

2.1.3 Thermodynamics for the photocatalytic reduction of CO_2 over TiO_2

In a photoelectrochemical cell, when incident light illuminates TiO_2, electrons (e−) and positive holes (h+) are formed (2.3):

$$2TiO_2 \xrightarrow{hv} e_{cb}^{-}(TiO_2) + h_{vb}^{+}(TiO_2) \qquad 2.3$$

Thereby, exciting and cleaving bonds of Ti^{4+} to Ti^{3+} as below (2.4):

$$\left[(Ti^{4+} - O^{2-}) \xrightarrow{hv} (Ti^{3+} - O^{-})^{*}\right] \qquad 2.4$$

Those generated charges are kept separated by the electric field created within the semiconductor because of band bending (as explained in Section 2.1.2 and shown in Figure 1.6). Holes interact with water adsorbed on the catalyst surface, leading to O_2 and H^+ evolution (2.5).

$$2H_2O + 4h^{+} \xrightarrow{hv(Ti^{3+}-O^{-})^{*}} 4H^{+} + O_2 \qquad 2.5$$

H^+ ions and CO_2 molecules then interact with the generated electrons, to form $^{\bullet}H$ radicals and $^{\bullet}CO^{-2}$ radical, respectively (2.6 and 2.7).

$$H^{+} + e^{-} \xrightarrow{hv(Ti^{3+}-O^{-})^{*}} {}^{\bullet}H \qquad 2.6$$

$$CO_2 + e^{-} \xrightarrow{hv(Ti^{3+}-O^{-})^{*}} {}^{\bullet}CO_2^{-} \qquad 2.7$$

The $^{\bullet}CO^{-2}$ (carbon dioxide anion radical) may go through an array of reactions with the $^{\bullet}H$ (hydrogen radical), as depicted earlier in Figure 1.7. These photocatalytic reactions involve eight electron transfers and may follow one or a combination of the equations below to result in a crowd of different products.

$$^{\bullet}CO_2^- + 8\,^{\bullet}H + h^+ \xrightarrow{(Ti^{3+}-O^-)^*} CH_4 + 2H_2O \quad 2.8$$

$$^{\bullet}CO_2^- + 6\,^{\bullet}H + h^+ \xrightarrow{(Ti^{3+}-O^-)^*} CH_3OH + H_2O \quad 2.9$$

$$^{\bullet}CO_2^- + 2\,^{\bullet}H + h^+ \xrightarrow{(Ti^{3+}-O^-)^*} CO + H_2O \quad 2.10$$

$$^{\bullet}CO_2^- + 2\,^{\bullet}H + h^+ \xrightarrow{(Ti^{3+}-O^-)^*} HCOOH \quad 2.11$$

$$^{\bullet}CO_2^- + 4\,^{\bullet}H + h^+ \xrightarrow{(Ti^{3+}-O^-)^*} HCHO + H_2O \quad 2.12$$

$$2\,^{\bullet}CO_2^- + 12\,^{\bullet}H + 2h^+ \xrightarrow{(Ti^{3+}-O^-)^*} C_2H_5OH + 3H_2O \quad 2.13$$

To make matters even worse, TiO_2 is a semiconductor and its photocatalytic property is also affected by its band-gap and wave length and intensity of the light used. Other factors include:

- pH;
- pressure;
- temperature;
- CO_2/H_2O mole ratio;
- formed intermediates that act as precursors for other products. Thereby, affecting the final selectivity of the products formed;
- duration.

Modifying TiO_2 with plasmonic metal co-catalysts such as Cu [24], is also an approach used to improve light absorbance and enhance charge separation (Figure 2.10). Thereby, improving the reaction kinetics for CO_2 reduction. (more on that in Section 2.4)

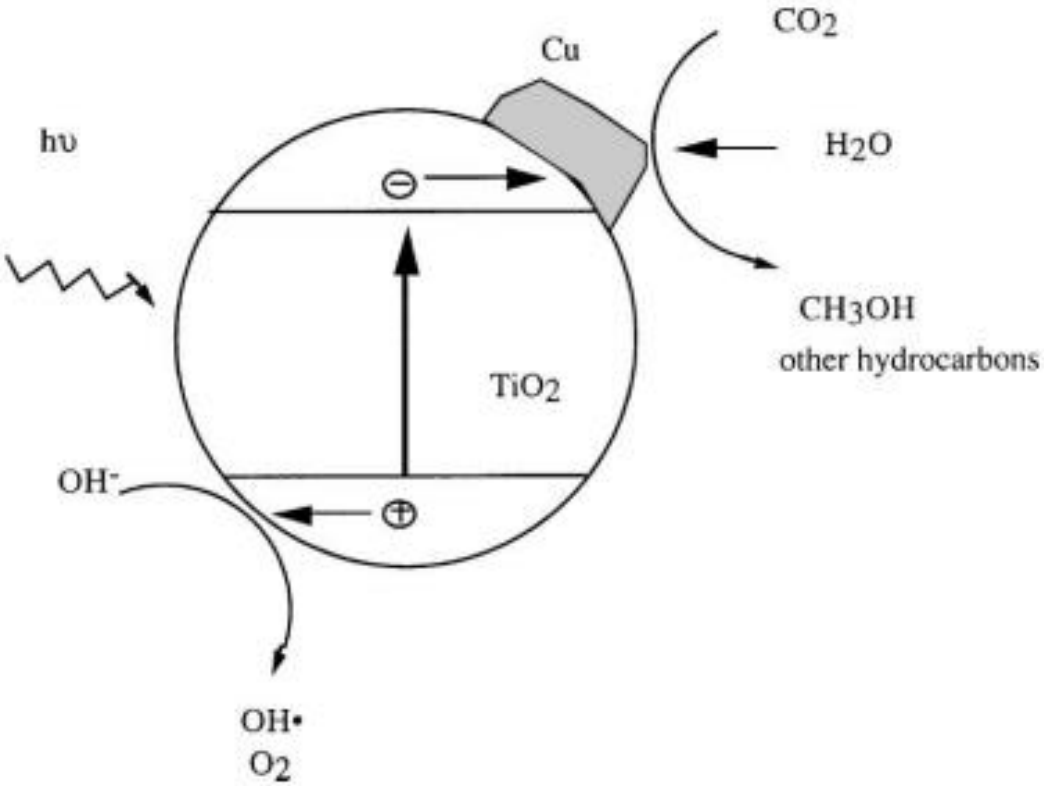

Figure 2.10 Schematic showing the reduction of CO_2 on Cu/TiO_2 system [25]

2.2 Anodization of Titanium

There are many techniques that result in size controlled, well ordered TiO_2 nanotubes (TNTs). The first TNTs were fabricated using a nanotube template. The template was a porous alumina layer made by anodizing an aluminum foil substrate [26]. Then the TNTs were deposited in the template by electrochemical deposition and the template was dissolved. Another method is the direct anodization of a titanium metal foil. In this process, the metal foil is oxidized when connected as anode in a two-electrode setup. When this oxidation takes place in an appropriate electrolyte, the process leads to nanotubes. Fluoride based electrolytes are used to etch TiO_2 leaving behind an array for TNTs on top of the titanium substrate [27, 28]. Nanotube length, thickness and pore size are affected by applied voltage, anodization time, temperature, electrolyte composition.

The work of Zwilling and co-workers in 1999, revealed the importance of electrolyte composition and fluoride ion concentration on the morphology of the TNTs. They studied various electrolyte compositions on various metals (titanium, aluminum and titanium/aluminum). It was observed that fluoride ions cause the subsequent formation and dissolution of a TiO_2 layer on the Ti metal, resulting in the formation of TNTs. In the absence of fluoride ions, the formed TiO_2 layer don't not dissolve and no nanotubes were formed [29].

Later work studied the effect of pH and electrolyte base (aqueous and non-aqueous electrolytes). Studies showed that a neutral pH allows tubes to reach >2µm in length. This is particularly interesting because tube length in aqueous acidic media, is limited. It is limited/short because the high currents observed in aqueous electrolytes results in faster etching/dissolution and shorter tubes. However, neutral pH helps slow down this dissolution resulting in longer tubes [30-33].

Alternatively, the use of non-aqueous organic electrolytes also influences the length and morphology of the TNTs. For non-aqueous organic electrolytes, the absence of both water and high conductivity leads to reduced oxide formation and dissolution when compared to aqueous electrolytes. Additionally, the higher viscosity of non-aqueous organic electrolytes reduces ion movement inside the tubes leading to smoother tube walls [27, 30-32, 34], shown in Figure 2.11.

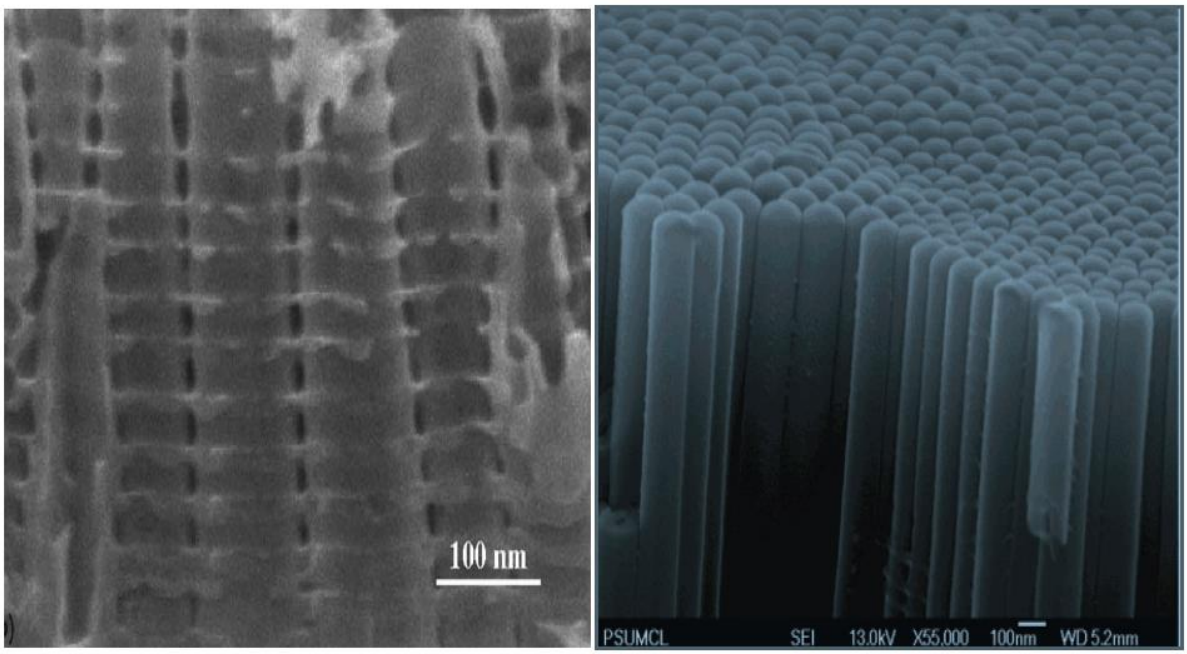

Figure 2.11 SEM images of (a) aqueous and (b) non-aqueous TNTs [32]

2.2.1 Anodization parameters

As mentioned above, nanotube length, thickness and pore size are affected by many factors such as applied voltage, anodization time, temperature, electrolyte composition. These parameters have been investigated in many studies.

Many parameters overlap in their effect on the final structure. Therefore; while keeping all other parameters constant (as explained above); electrolyte type, pH and Fluoride concentration affects the rate of oxide formation and dissolution. Constant voltage is used to control the diameter of the tube. The result are size uniform tubes with large pore size at higher voltages and small pores at lower voltage [29]. On the other hand, constant current leads to tubes of non-uniform diameter because of the changing voltage needed to maintain a constant current [27]. Finally, duration of anodization and tube length are directly proportional [32, 35-37].

2.3 Ordered TiO_2 Nanotube arrays in photocatalysis

To harvest more of the sun's energy, the material's thickness needs to be large. However, in the bulk the distance travelled by the holes to the surface of TiO_2 (to oxidize water) is relatively increased as shown in Figure 2.12(a). This in turn increases the chances of recombination, especially if the material is rich in defects. One nanostructure solves this problem. One-dimensional nanostructures can offer the depth needed to harvest the sun's energy while allowing the generated holes to travel a short distance (in the range of nm) to the surface, as shown in Figure 2.12(b). Thereby, uncoupling the two processes of charge collection and generation that are coupled in bulk structures.

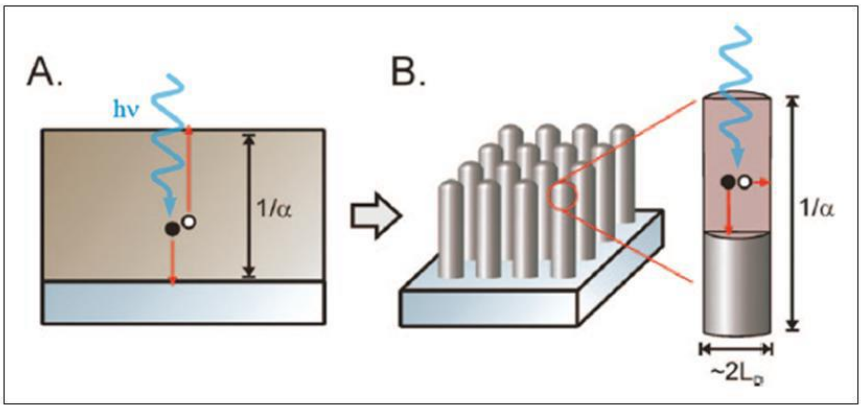

Figure 2.12 Comparison of (a) bulk and (b) 1D nanostructures in decoupling of charge generation and charge collection [38].

In Figure 2.12(b), the longest distance travelled by a generate charge is from the center of the tube of radius L_D. Where: L_D is the diffusion length in meters; D is the diffusivity in m²/s and τ is the lifetime in seconds.

$$L = \sqrt{D\tau}$$ *Equation 2-14*

The diffusion length of a material is a very important parameter in nanotube synthesis. Ideally, the thickness of the tube wall needs to not be greater than $2L_D$ to avoid recombination.

2.3.1 Modifying TiO_2 nanotubes

While TiO_2 is well known for its oxidative properties and excellent stability in aqueous media, its wide band-gap limits the absorption of this semiconductor to the UV region of the light spectrum. It was shown by S. Sakthivel *et al.* [39] that metal decorated TiO_2 can absorb more light and get excited by lower energies. This is due to the localization of the metal's energy levels within the TiO_2, where the VB electrons of the metal can then be easily excited into the CB of TiO_2 as was previously discussed in Section 2.1.1 and shown in Figure 2.13. Another benefit to this localization effect is, less recombination.

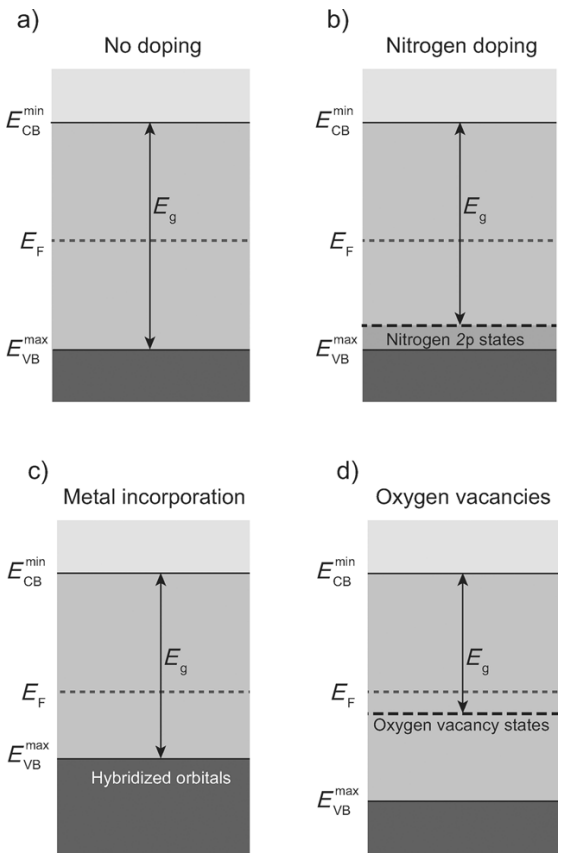

Figure 2.13 Semiconductor (a) without any doping, (b) with Nitrogen doping to narrow the band-gap by introducing states above the VB, (c) Incorporation of metal dopants leads to hybridization of orbitals and a higher VB, (d) narrowing of the band-gap by inducing oxygen vacancies to introduce impurity states below the E_F [40].

An alternative class of solar energy conversion materials is transition metal oxynitrides. Since metal-nitrogen bond has higher potential energy than metal-oxygen bond, oxynitrides [41-48] have narrower band gap energies compared to their metal oxides counterparts. Additionally, oxynitrides are stable in alkaline media making them ideal water splitting photoelectrodes [41-44]. Particularly, titanium oxynitride (TiON) is a promising material for visible light absorbtion and appropriate band-edge positions for water splitting [45-48]. Vitiello *et al.* [46] used NH_3 nitridation to fabricate TiON nanotube arrays from anodized Ti foil. Their TiON showed enhanced photoelectrochemical properties and significant visible light response. Efficient nanostructured mesoporous TiON thin films were reportred by Ferrero *et al.* [47]. The films resulted in a shift of the titania absorption edge, due to the introduction of N atoms. Alternatively, Kim *et al.* [48] used Ti-N substrates to fabricate Ti-O-N nanotubes *via* anodization, resulting in a significant visible light photoresponse. Asahi *et al.* [49] reported that N-doped TiO_2 has an influence on the photocatalytic activity for the decomposition of acetaldehyde and methylene blue at wavelengthes up to 550 nm. Recently, Gebauer *et al.* [50] have investigated the oxygn reduction reaction (ORR) on N-doped titanium dioxide. It was found that N-doped titanium oxide significantly improve the ORR performance compared to non-doped TiO_2. Decorating TiON materials with nanoparticles and/or sensitizers [51, 52] has also been recently proposed as an effective method to enhance the surface catalytic activity of a plethora of materials [53-56]. Hiroaki *et al.* [54] have examined the effect of Ag nanoparticles (NPs)-decorated TiO_2 nanotube arrays. This hybrid device resulted in higher photocatalytic activity and solar energy conversion efficiency (~ 3.5 μA) compared to bare TiO_2 electrode (~ 0.5 μA) [54-56].This enhanced catalytic effect was related to the formation of hydroxyl radicals, which were made possible through better charge-transfer processes [57, 58].

In summary, amongst the many material requirements for photoelectrochemical reactions the two most important are (i) a well-suited band-gap that is narrow enough to absorb maximum light (≈2 eV) and is well positioned (as explained above) to allow theses generated electron/hole pairs to split water (ii) minimizing bulk and surface recombination's by lowering material defects and facilitating faster charge transport. The wide band-gap of TiO_2 is well suited for this band-gap engineering. That is why research is still ongoing to reach an optimum efficiency though the metal decoration of TiON nanotubes.

2.4 Photocatalytic Reduction of CO_2 over TiO_2

Carbon dioxide is a very stable molecule and its reduction requires the input of high energy in the form of temperature and pressure. However, since CO_2 can be activated by light there is huge potential for its the photocatalytic reduction. The first study of the photocatalytic reduction of CO_2 in water was conducted in 1997, using TiO_2 and various other semiconductors [20]. The studies were run under mercury and xenon lamps. The products of the reduction were formaldehyde (HCHO), formic acid (HCOOH), methyl alcohol (CH_3OH), and trace amounts of methane (CH_4). SiC gave high yields of formaldehyde and methyl alcohol. This is observed in SiC because its CB edge is more negative than the HCHO/ H_2CO_3 redox potential (Figure 2.14). However, this is not observed in WO_3 where the CB is more positive than the HCHO/ H_2CO_3 redox potential and methyl alcohol is absent [59]. Similar wide band-gap material such as $SrTiO_3$ were studied by Halmann *et al.* [60]. $SrTiO_3$ has CB at a more negative potential (vs NHE) than the redox potential of CH_3OH/H_2CO_3. Therefore, excited electrons of $SrTiO_3$ can reduce carbon dioxide. This further stress the importance of band edge positions for CO_2 reduction as well. Halmann *et al.* [61] also studied the effect of doping TiO_2 with metals such as Cr, V and Ru. Due to the shifting of the energy bands, there was an observed increase

in the production yields of methanol, formic acid and formaldehyde, when doping with Ru. The complex cascade of reactions, as described in Section 2.1.3, leads to a horde of products that are sometimes stable or unstable and may transform to other products that may be quantifiable or not. The position of the CB (where all the photogenerated electrons reside) vs the redox potential (of the products to be formed) is one but not the only factor in this complex reactant system.

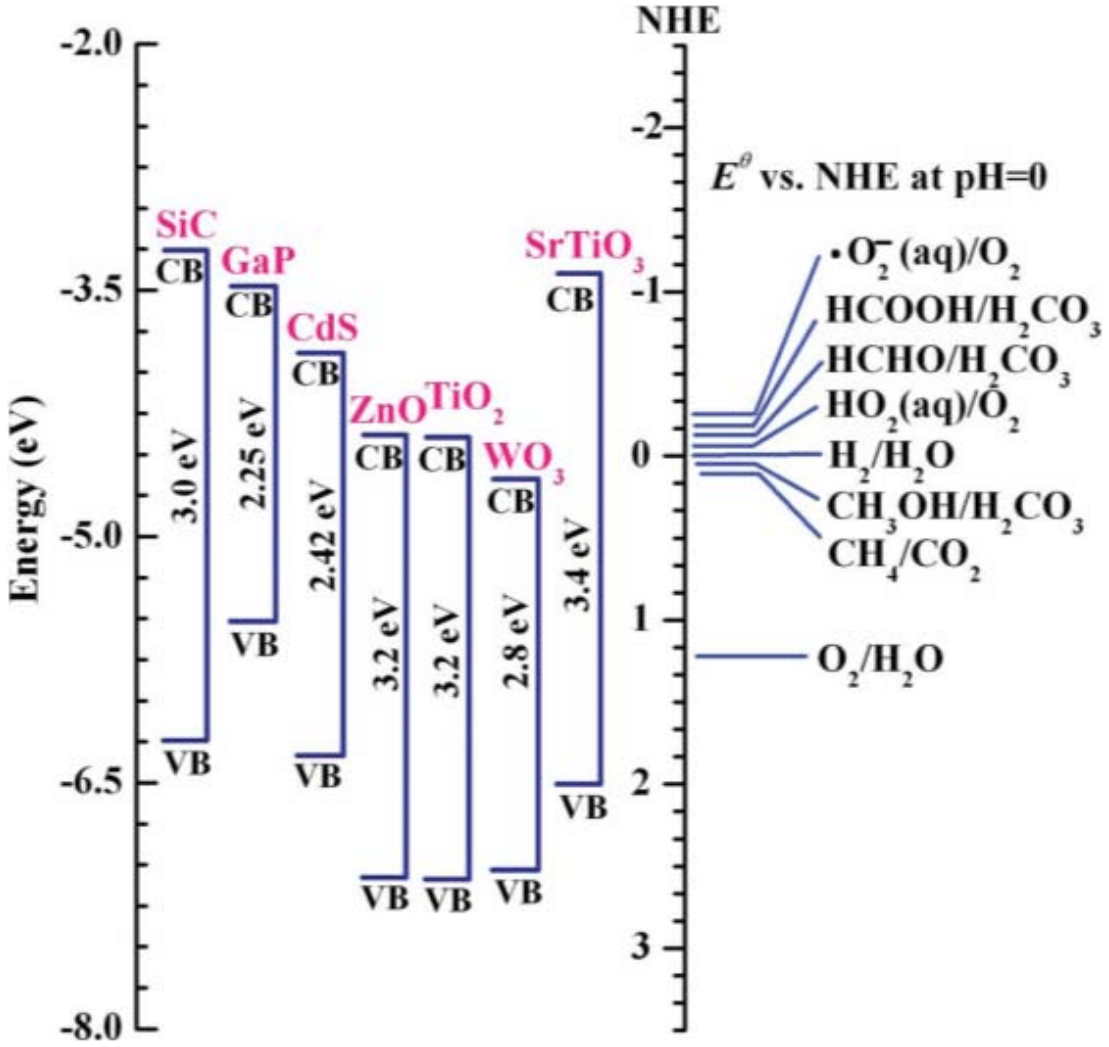

Figure 2.14 Various semiconductors used in CO_2 reduction and their conduction and valence band positions at pH 0 relative to NHE [62]

Anatase TiO_2 was studied as a photocatalyst for the reduction of CO_2. The large band-gap catalyst was found to be effective in methane formation, but the reaction depended on a few

variables: (i) temperature, (ii) H_2O/ CO_2 ratio, (iii) type of metal catalyst used. It was observed that the best H_2O/ CO_2 ratio was 5:1 and that the addition of Pt metal catalyst increased the yield of methane compared to methanol. A further study of the reaction intermediates was conducted and revealed that methane formation likely resulted from the reaction between carbon radicals and hydrogen [63, 64].

2.4.1 Copper as catalyst

In the early CO_2 reduction work of Hiro *et al.*, it was shown that there is a difference between Cu and Ni product selectivity: on Cu, suitably negative potentials (>1V vs RHE) are needed to produce CH_4, while at those highly negative potentials H_2 is predominantly evolved on Ni surfaces. Figure 2.15 shows the product distribution and current efficiency on Cu surfaces, with methane and hydrogen being the dominant products at higher potentials [65].

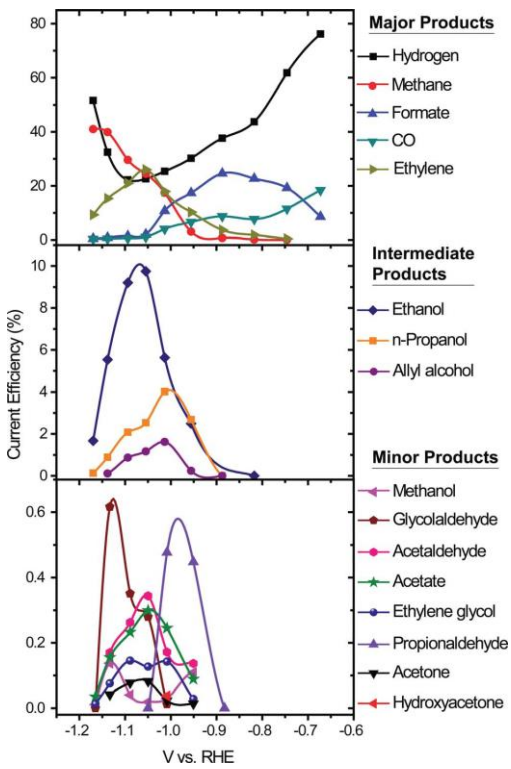

Figure 2.15 Current efficiency of products formed from the electrochemical reduction of CO_2 on Cu surfaces [65].

Copper is on top of a volcano-type relationship between metals for their theoretical overpotential and Ni is an excellent cost-effective alternative to Pt for Hydrogen evolution (shown in Table 2.1). Researchers have since turned to alloying as a means of reducing this overpotential. Alloys of Cu with Sn, Pb, Zn, Cd, and Ag were studied [66]. The alloys highly influenced the selectivity and overpotential.

Table 2.1 Faradic yields of various metal catalysts as reported by Hori et al. [67].

		Faradaic yield, %				
electrode	V vs RHE	hydrocarbons/ organics[a]	CO	HCOOH	H_2	total
Ni	−1.09	2.1	0.0	1.4	88.9	92.4
Cu	−1.05	72.3	1.3	9.4	20.5	103.5
Pd	−0.81	2.9	28.3	2.8	26.2	60.2
Ag	−0.98	0.0	81.5	0.8	12.4	94.6
Pt	−0.68	0.0	0.0	0.1	95.7	95.8
Au	−0.75	0.0	87.1	0.7	10.2	98.0

The exploration of materials that meet the requirements for efficient CO_2 reduction is a challenge. It is clear from Figure 2.15, that hydrogen evolution is an important precursor for hydrocarbon formation. In Figure 2.15, hydrogen evolution precedes all other hydrocarbon formation. It also declines as hydrocarbon yield rises, signifying that the formed hydrogen is channeled towards hydrocarbon formation.

2.4.2 Metal-doped TiO_2

The effect of Cu as a co-catalyst to CO_2 reduction was then studied. In 1994, Adachi *et al.* [68] studied the effect of Cu loading on TiO_2 powder. The powder was suspended in a saturated and pressurized CO_2 solution and illuminated with a Xenon lamp. The products formed were methane and ethylene. When the Cu loading was increased to 2.0 wt.% methanol was observed at 118 µmol/g after 6 hours of UV lamp illumination [69]. This yield was even higher than sol-gel TiO_2 and TiO_2 P25. Similarly, as shown in Figure 2.16 the addition of Cu oxides to TiO_2 allows the reduction of CO_2 to various hydrocarbons.

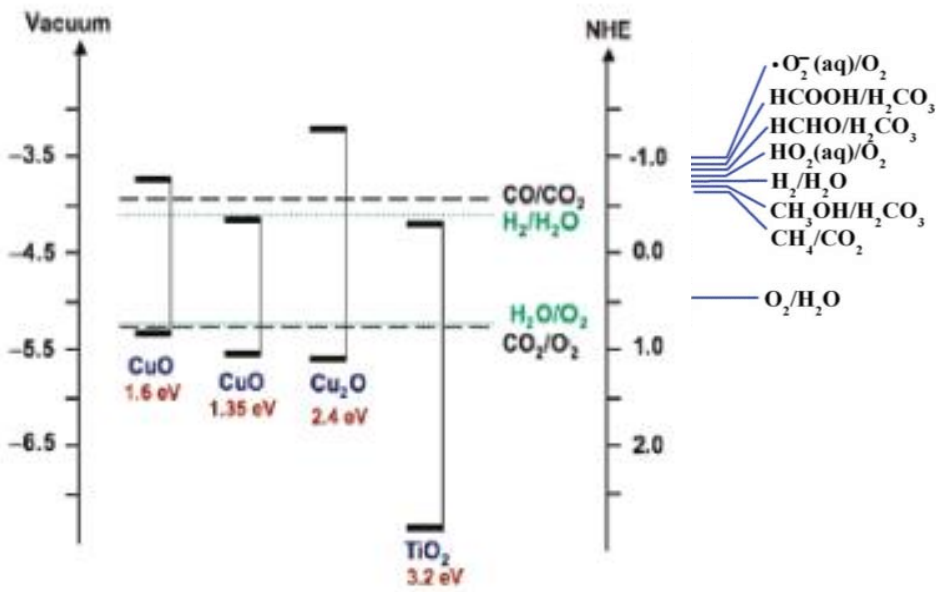

Figure 2.16 Band-gap alignment for Cu/TiO_2 systems [70]

It is important to understand how the Schottky barrier created in a metal/semiconductor system helps trap electrons and results in the redistribution the electric charge. Figure 2.17 shows the Schottky barrier created in n-type and p-type semiconductor systems with a low work function and high work function metals. Figure 2.17 (c) is an illustration of the Cu/TiO_2 system, where electron trapping in Cu is observed as the generated electrons from TiO_2 move into the metal and thereby reducing recombination with the holes. As a result, the quantum efficiency was 10 % and the energy efficiency was 2.5%.

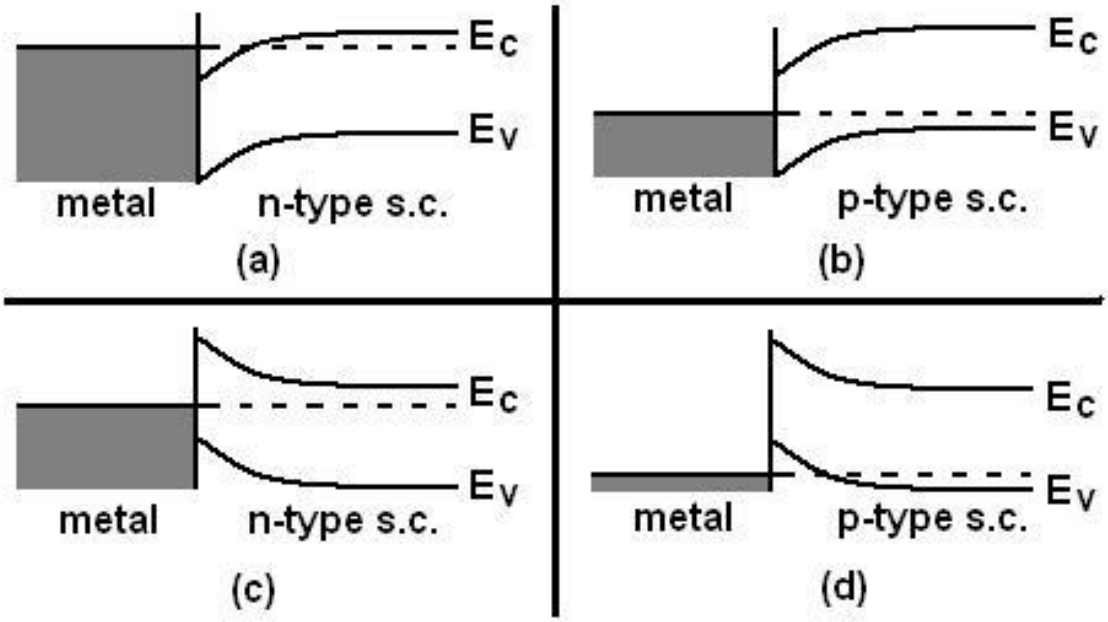

Figure 2.17 (a) and (b) are low work function metals with n-type and p-type semiconductors, respectively. (c) and (d) are high work function metals with n-type and p-type semiconductors, respectively [71].

It is also suggested that Cu_2O, as a dopant, is the most effective electron trapper. The Cu^+ state in Cu_2O has the highest positive potential and is therefore effective as an electron trapper. This however is a double-edged sword, because the dopants with the most positive potential will attract the electrons and this may make it difficult for the electrons to travel on the catalyst surface and hence lead to electron/hole recombination [72].

In literature, 1D nanotube arrays of N_2 doped TiO_2 decorated with Cu and/or Pt nanoparticles were also studied in the reduction of gaseous phase CO_2 with water vapor (Figure 2.18). The reported methane yield was 160 µL/gh amongst other hydrocarbons, following the chemical pathways proposed in Figure 2.19. This high yield was attributed to (i) the enhancement in light harvesting offered by the Cu and Pt nanoparticles; (2) the increase in surface area of the material due to 1D nanotubes, (iii) and the unique ability of TiO_2 nanotubes to be long enough to absorb enough light to generate charges but also provide a wall thinness that is thin enough for those charges to interact with reactants before recombination. The quantum efficiency was about 0.74% [24].

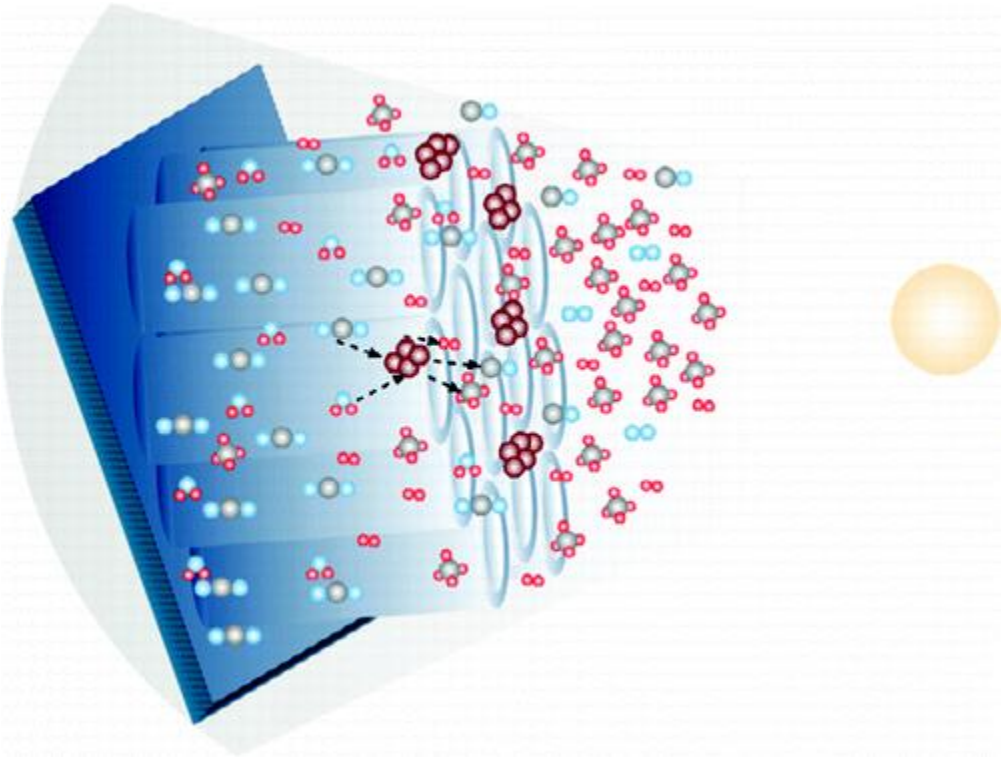

Figure 2.18 One-dimensional TION nanotubes decorated with Cu nanoparticles surrounded by water vapor and CO_2 under direct sunlight to for reduced products without external bias.[24]

$$TiO_2 + h\nu \longrightarrow TiO_2^* \, (e^-_{cond} + h^+_{val})$$

for an oxidation

$$H_2O \xrightarrow[TiO_2,\,Cu]{h\nu} 2H^+ + 1/2O_2$$

for reductions

$$CO_2 \xrightarrow[TiO_2]{h\nu} CO \xrightarrow[TiO_2]{h\nu} {}^{\bullet}C \xrightarrow[TiO_2,\,Cu]{2H^+ + 2e}$$

$${}^{\bullet}CH_2 \xrightarrow[TiO_2,\,Cu]{2H^+ + 2e} CH_4$$

$${}^{\bullet}CH_2 \xrightarrow[Cu]{{}^{\bullet}CH_2} C_2H_4$$

Figure 2.19 Proposed reaction of water splitting and CO_2 reduction on TiO_2 surface catalyzed with Cu [68]

2.4.3 Bimetallic-doped TiO_2

Many metals have been studied as electrochemical catalysts for CO_2 reduction [14, 73]. One of the prominent metal electrocatalysts is Cu. As reported by Hori, for Cu CO formation dominates at relatively low overpotentials (above -1.2V NHE), while other hydrocarbons are formed at more negative potentials [74]. An appealing property to Cu, is its high faradic efficiency towards methane and ethylene formation. However, Cu tends to be very sensitive to impurities in the electrolyte. These impurities lead to the reduction in the methane yield.

Another widely studied catalyst is Nickel. It is a cheaper alternative to platinum due to its high hydrogen evolution activity at low overpotentials and its high CO adsorption strength in aqueous solutions. However, the high CO adsorption strength limits the long-term reduction of CO_2 at the surface [75]. It is also interesting to note that in comparison to Ni, Cu has a much weaker CO adsorption strength. Although Ni and Cu have many appealing properties as electrocatalysts, individually both metals have longevity and stability problems [74].

Bimetallic TiO_2-based electrocatalysts have been receiving a lot of attention lately because they were shown to possess several advantages over metal electrocatalysts such as: (1) improving the stability of CO_2 reduction activity, which effectively solves the problem of metal electrocatalysts, (2) the ability to direct product selectivity [75], (3) their allowance for new and interesting properties resulting from the synergy of two metals [76], and (4) their abundance and low prices. Bimetallic electrocatalysts are considered a promising alternative to metals. For instance, alloying platinum with another metal can enhance its photocatalytic performance in terms of activity and selectivity, furthermore, bimetallic platinum is

significantly cheaper than pure platinum [76]. Another example is Cu-Au alloy, it appears that increasing Au amount leads to an increase in CO formation in aqueous solutions [77].

Titanium dioxide co-doped with bimetallics was studied in 2011. Bimetallic TiO_2, co-doped with Cu and Ce was prepared by equivalent-volume incipient wetness impregnation and studied for the photocatalytic reduction of CO_2. Methanol production reached 180.3 µmol/g of catalyst. This enhanced effect was attributed to the activation of H_2O and CO_2 molecules by Ce. Whereas, Cu acted as a channel of photogenerated electron thereby preventing recombination [78].

In summary, wide band-gap semiconductors such as TiO_2 are also perfectly suited for the photocatalytic reduction of CO_2, because their VBs and CBs are sufficiently more negative and more positive than the oxidation and reduction potentials of CO_2 in water. However, the requirement to using wide band-gap semiconductors is high light energy and this can be adjusted with the addition of co-catalysts that (i) help shift the absorption spectrum of the semiconductor (ii) tweak the selectivity of the formed products to yield usable hydrocarbons such as methanol and methane.

2.5 Scope and Objectives of the Thesis

The scope of this thesis is to enhance the properties of semiconductors to split water and produce hydrogen. This generated hydrogen maybe collected and used as fuel, or it can be further used in the reduction of carbon dioxide into various hydrocarbon fuels. The current semiconductor technologies resort to (i) doping as a means of narrowing the band-gap and enhancing light absorption (discussed earlier in Section 2.1.1) or (ii) decoration with metals to enhance charge separation, as depicted in Figure 2.20b and c.

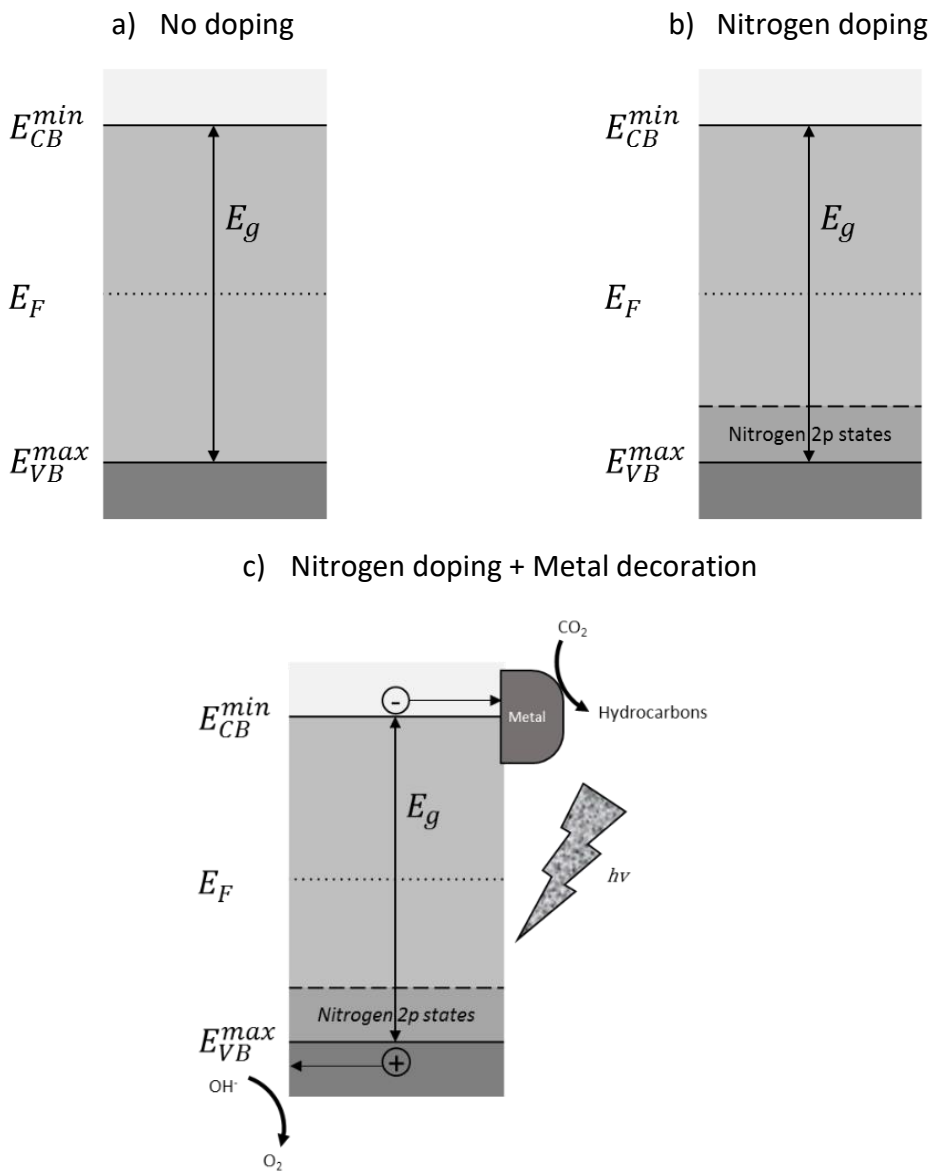

Figure 2.20 Illustration of semiconductor band-gap engineering

To the best of our knowledge, there are no reports in literature on the synergistic effect of doping TiO_2 to modify the band-gap and increase light absorption, while also decorating it with metal nanoparticles to enhance charge separation. Therefore, the logic question was: Can this synergism improve water splitting efficiency and tweak the selectivity of CO_2 reduction catalysts towards usable hydrocarbons?

Chapter 3: Defines the experimental procedures used to synthesize and characterize the Ag-decorated TiON and Cu-Ni TiON nanotubes for water splitting and CO_2 reduction, respectively.

Chapter 4: Presents and discusses the obtained results for the Ag-decorated TiON for water splitting.

Chapter 5: Presents and discusses the obtained results for the Cu-Ni for CO_2 reduction.

Chapter 6: Mentions the important highlights of the work and discusses plans for future work.

Chapter 3: Experimental

3.1 Materials and methods:

3.1.1 Ag-decorated TiON nanotubes

Titanium foil (0.25 mm thick, purity 99.8 %) was cut into portions and polished and cleaned by ultrasonication in acetone, ethanol and deionized water, respectively. Two- electrode electrochemical cell was used for anodization in which the Ti metal foil (positive electrode) and a platinum coil (negative electrode) were connected to a DC power supply at 30 V (Figure 3.1). Ethylene glycol-based solutions containing 0.5M NH_4F and 3ml H_2O (optimized experimentally). All samples were anodized for 120 minutes at room temperature.

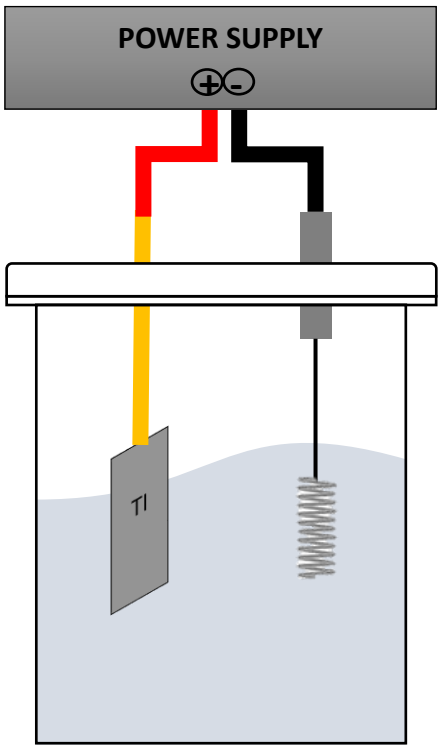

Figure 3.1 Anodization Setup

The resulting titanium oxide nanotubes were then annealed in ammonia flow (200 sccm) at 600 °C for two hours. The heating and cooling rates were as low as 2 °C/min to preserve the

nanotubular architecture and avoid their detachment. As a reference, titanium oxide nanotubes sample was annealed in air (450 °C and 2 °C/ min for 2 hours).

The Ag nanoparticles were prepared by the borohydride reduction method. A 100 ml of 1 mM $AgNO_3$ (Sigma-Aldrich, 99,999 %) was added to a mixture of 30 ml of 2 mM $NaBH_4$ (Sigma-Aldrich, 98 %) under vigorous stirring. For the preparation of Ag decorated TiON nanotube arrays, 50 µl of Ag colloidal solution (the loading density is 3.42 x 10^{11} Ag NPs per 1 cm^2 foil) was drop-casted onto the TiON foil and left to dry overnight (Figure 3.2).

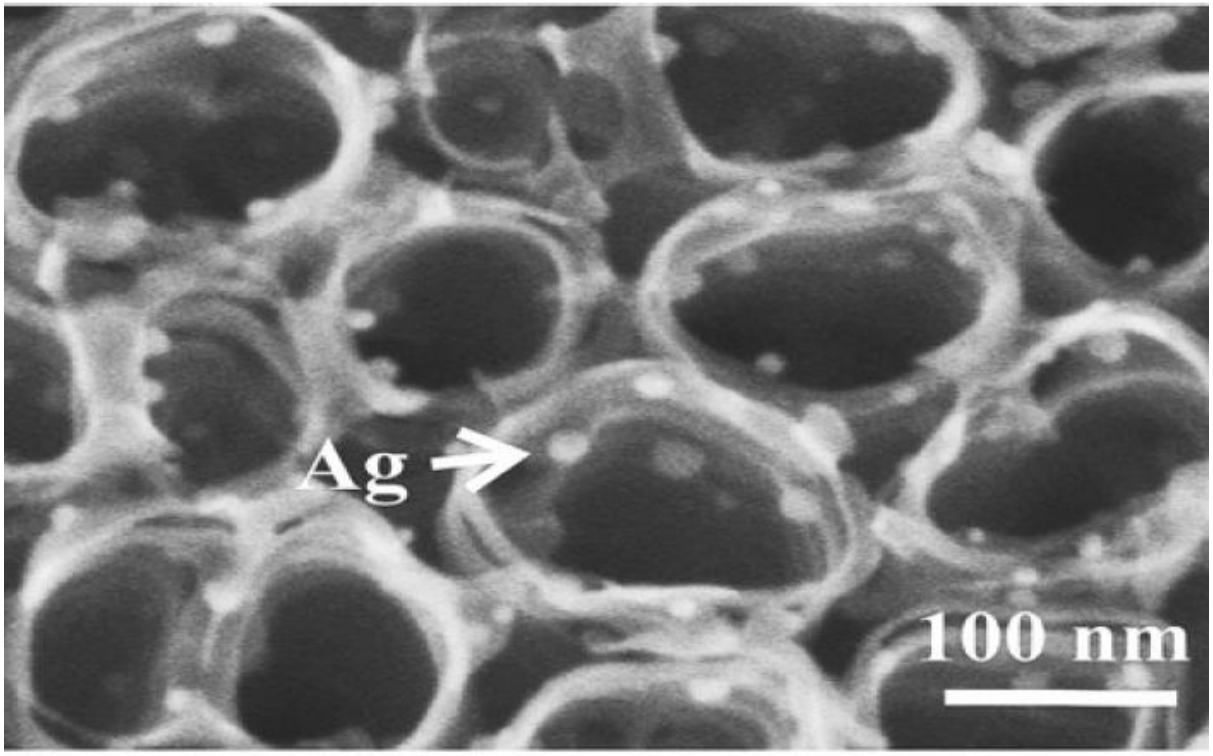

Figure 3.2 Ag decorated TiON nanotubes

3.1.2 Cu-Ni alloys for the CO_2 reduction

High purity Cu-Ni samples were received with varying ratios as listed in Table 3.1

Table 3.1 Cu to Ni ratios of samples used

	Atomic Ratio	
	% Cu	**% Ni**
Cu	100	-
5% Ni	95	5
10% Ni	90	10
30% Ni	80	20
70% Ni	25	75
Ni	-	100

Samples were polished with fine emery paper then electropolished in 85% phosphoric acid solution at room temperature for 5 minutes. Samples were held at 4 volts for 5 minutes using titanium as the counter electrode.[74] The samples were then double rinsed with distilled water and dried under a nitrogen stream.

3.2 Characterization

3.2.1 Ag-decorated TiON nanotubes

Field emission scanning electron microscopy (FESEM) images and energy dispersive X-ray spectroscopy **(**EDX) measurements were carried out using a FEI electron scanning microscope in the Yousef Jameel Science and Technology Research Center (YJ-STRC) at the American University in Cairo. The powder Glancing Angle X-ray diffraction (GAXRD) measurements were carried out at room temperature using Rigaku Miniflex II diffractometer with Cu KαR radiation

at 30 kV and 20 mA between 2θ angles of 20 and 80° with scanning rate of 0.025^{o} per step per second**.** X-ray photoelectron spectroscopy (XPS) measurements were carried out on Kratos Axis Ultra XPS with a monochromatic Al Kα radiation source (1486.6 eV) in a UHV environment (ca. $5x10^{-9}$Torr). Transmission electron microscopy (TEM) images were acquired by a FEI Philips Technai 20 transmission electron microscope with an accelerated voltage of 200 kV. The optical absorption of the samples was measured using a Cary 5000 UV-Vis-NIR spectrophotometer. The *J-V* measurements were carried in a three-electrode electrochemical cell with a saturated calomel electrode (SCE), a platinum wire and the tested sample were used as reference, counter, and working electrodes, respectively. The area of the working electrode was 0.88 cm^2 and that of the counter electrode was 3.15 cm^2. The working electrode was immersed in 0.1 M KOH (Carl-Roth, Germany 99.98 %). The KOH solution was prepared from ultrapure water (18.2 MΩ cm at 25 °C, TOC < 1 ppb) and was purged with nitrogen gas during the measurement. A scanning potentiostat (Gamry 3000) was used to measure dark and illuminated currents at a scan rate of 10 mV/s. A 100 W ozone-free xenon lamp (Abet Technologies, USA) was used as the light source, with an AM 1.5 G filter to simulate sunlight at 100 mW/cm^2.

3.2.2 Cu-Ni alloys for the CO_2 reduction

X-ray spectroscopy **(**EDX) measurements were carried out using a FEI electron scanning microscope. The powder Glancing Angle X-ray diffraction (GAXRD) measurements were also carried out at room temperature using Rigaku Miniflex II diffractometer with Cu KαR radiation at 30 kV and 20 mA between 2θ angles of 20 and 80° with scanning rate of 0.025° per step per second.

Electrochemical measurements were conducted in a two-compartment glass H-Cell as shown in Figure 3.3. The glass cell was soaked in Aqua Regia (2:1, $HCl:HNO_3$) overnight then boiled vigorously in water to remove any metal or carbon traces that may interfere with the results. The compartments were separated by a proton exchange membrane (Nafion 117) to avoid products in the working compartment from mixing and oxidizing at the counter electrode. The nafion membrane was cleaned by boiling it in 3%vol H_2O_2 solution for 1 hour. The catholyte was prepared using 60mls of 0.1M KOH aqueous pre-electrolyzed solution saturated with 99.99% CO_2 gas. The pre-electrolysis and saturation with CO_2 gas were run overnight, simultaneously. The pre-electrolysis ensured that any trace metals in the prepared saturated solution were removed and the resultant solution was of high purity. The anolyte was 60mls of 0.1M KOH aqueous pre-electrolyzed but not saturated with CO_2 gas. The potential of the cathode was held with respect to an Ag/AgCl reference electrode.

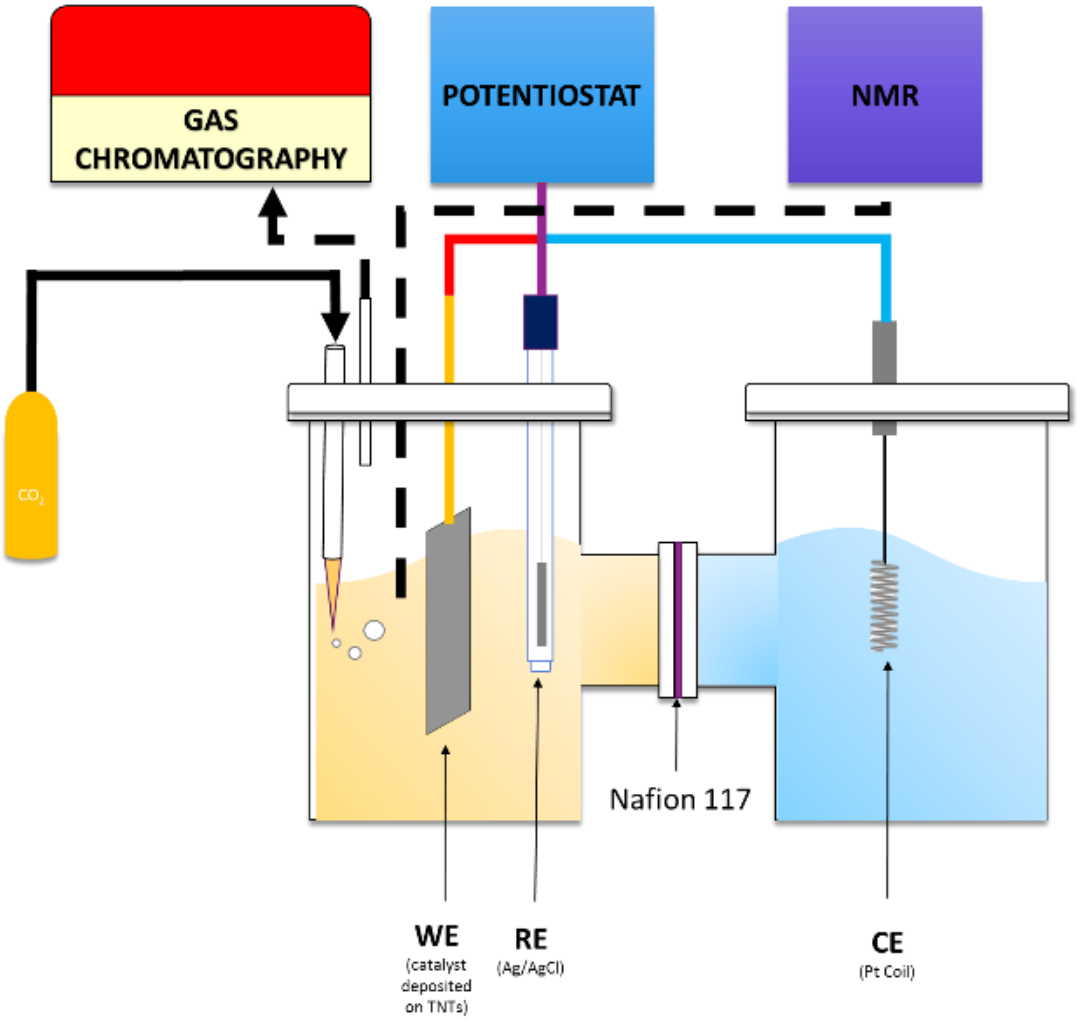

Figure 3.3 CO_2 electrochemical reduction setup

Linear Sweep voltammetry (LSV) was used to gain insight on the reduction reaction at various potentials. The potential was scanned at a sweep rate of 50 mV-s^{-1} from 0.2V to -1V NHE. This information can be very telling of reaction onset potentials and used to identify overpotentials and compare samples. Chronoamperometry was used to fix potential at a stationary electrode in an unstirred solution and the current produced was studied over a period.

Chapter 4: Silver Nanoparticles-Decorated Titanium Oxynitride Nanotube Arrays for Enhanced Solar Fuel Generation*

Figure 4.1a, shows an FESEM top-view image of the fabricated titanium oxide nanotubes. The well-aligned, densely packed nanotube arrays that are several microns long were formed and distributed uniformly with full coverage on the film surface. The average length of the nanotubes is estimated as 11.2 ± 3 µm, while the inner diameter and the wall thickness are 50 and 15 nm, respectively. The morphology and structure of the nanotubes are preserved even after annealing in air (Figure 4.1a) or ammonia ambient for 2h (Figure 4.1b). Note that the nanotubular structure has not been affected by annealing, where the diameter is slightly increased into 54 nm and the wall thickness is 14±2 nm. Figure 4.1c shows the Ag nanoparticles-decorated nanotubes. Also, Figure 4.1d shows HRTEM image of the silver nanoparticles. To prepare such electrodes, 50 µL of Ag colloidal solution was drop casted onto the TiON foil and left overnight to dry at room temperature. Then, the Ag/TiON surface was washed with ultrapure water. Note that the Ag nanoparticles are well-dispersed on the TEM grid with uniform size (13 ± 2 nm) and spherical shape.

* This chapter was published as an article: Soliman KA, Zedan AF, Khalifa A, El-Sayed HA, Aljaber AS, AlQaradawi SY, Allam NK. Silver Nanoparticles-Decorated Titanium Oxynitride Nanotube Arrays for Enhanced Solar Fuel Generation. Scientific Reports. 2017 May 15;7(1):1913.

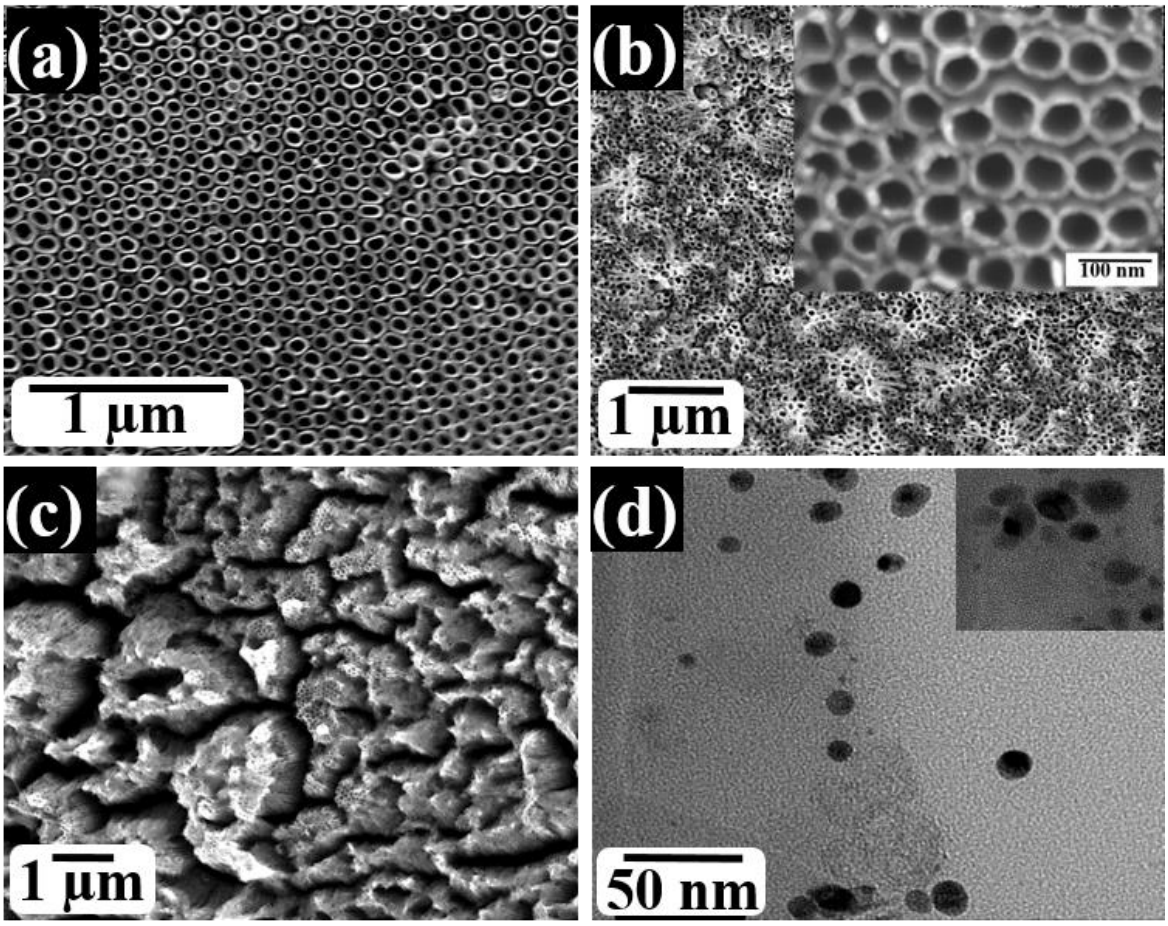

Figure 4.1 SEM images of (a) air-annealed, (b) ammonia-annealed, (c) Ag-decorated ammonia-annealed titanium oxide nanotube arrays, and (d) TEM image of the Ag nanoparticles deposited on carbon-coated copper grid.

To investigate the structure and composition of the fabricated nanotube arrays, EDX (Figure 4.2a), GAXRD (Figure 4.2b) and XPS (Figure 4.3) analyses were performed. Figure 4.2a, shows the EDX spectra for (i) air-annealed, (ii) ammonia-annealed, and (iii) Ag-decorated ammonia-annealed titanium dioxide nanotube arrays. The peak at 0.277 eV is related to carbon species, whereas the peak at 0.525 eV is related to oxygen species. Note that the intensity of the peak at 0.525 eV decreased after annealing in ammonia and another peak emerged at 0.392 eV, which is assigned to nitrogen atoms. The sharp peak at 2.984 eV is a good indication for Ag decoration on TiON nanotube arrays. The common peak around 4.508 eV belongs to titanium species. Figure 4.2b shows the GAXRD patterns of the nanotubes annealed in air and those annealed in ammonia, revealing crystalline structures of titanium oxide. The appearance of

the characteristic diffraction peaks at 25°, 38.1°, 47.8°, 52.8°, and 53.9°, corresponding to the (101), (004), (200), (105), and (211) facets, respectively elucidate the crystalline structures of titanium oxide [46]. Note that the peak at 2θ ~43° appeared in the GAXRD spectra of NH_3-annealed sample is assigned to TiN and corresponds to cubic titanium oxynitride as reported by Zukalova *et al.* [79]. Furthermore, the signature of the underlying Ti metal is apparent as indicated from the sharp peak at 40° [46]. Upon annealing in ammonia, the peaks are still located at the same angle, however the intensity of the peaks decreased (Figure 4.2b, ii). Note that both oxides and oxynitrides are usually having virtually overlapping GAXRD patterns [41-44].

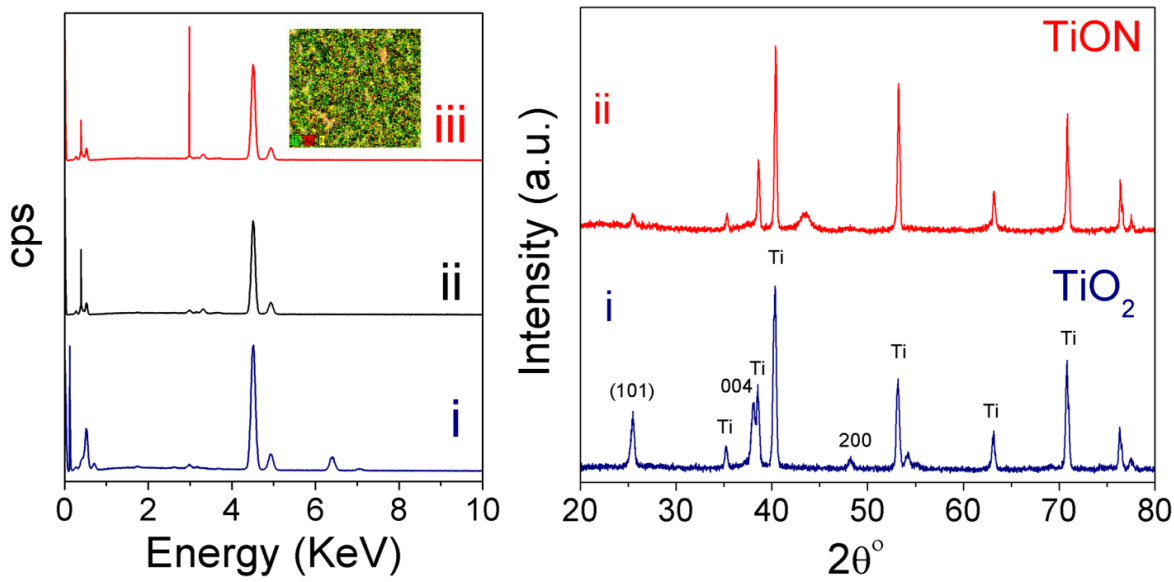

Figure 4.2 (a) EDX and (b) GAXRD spectra of (i) air-annealed, (ii) ammonia-annealed, and (iii) Ag-decorated ammonia-annealed samples. The inset in Fig. 2a is the EDS mapping for Ag nanoparticles.

As GAXRD could not distinctively confirm the formation of TiON nor the presence of the Ag nanoparticles. XPS being a surface sensitive technique, is believed to resolve the differences between the oxides and oxynitrides [42]. Figure 4.3 shows the XPS high-resolution scans of the four elements; Ti, O, N and Ag for air-annealed, ammonia-annealed, and Ag-decorated ammonia-annealed nanotube samples and the data are listed in Table 4.1. Figure 4.3a shows the Ti 2p XPS lines. The Ti 2p spectrum of the air-annealed TiO_2 sample

(Figure 4.3a i) exhibits two peaks at 458.5 and 464.3 eV characteristic of Ti $2p_{3/2}$ and Ti $2p_{1/2}$, with a spin orbit splitting of 5.8 eV, indicating Ti^{4+} oxidation state [47]. Upon annealing in ammonia (Figure 4.3a ii) and Ag decoration (Figure 4.3a iii), both peaks are shifted from their original positions, (Figure 4.3a ii, iii). The shift to low energy side is a signature of increasing electron cloud density around Ti. This can be related to the introduction of a less electronegative atom into the crystal lattice of TiO_2 and the incorporation of N (3.04 on Pauling scale compared to O 3.44 on Pauling scale) into titania.[80]. Figure 4.3b shows O1s XPS spectra acquired for air-annealed, ammonia-annealed, and Ag-decorated nanotube samples. The spectrum shown in Figure 4.3b-i exhibits small shoulder at 532.2 eV and a singlet peak at 531.4 eV. The peak at 531.4 eV is attributed to O-H groups, and the small shoulder at 532.2 eV can be attributed to physisorbed water [81]. The position of the shoulder shifted a little to lower binding energies after annealing in ammonia (ii, iii). Such shift caused by the increase of titanium in low valence states [81]. Note that the Ti $2p_{3/2}$ photoemission line at 458.5 eV is diagnostic for oxynitride (Ti-O-N) [81]. Figure 4.3c shows the N1s XPS spectra acquired for air-annealed, ammonia-annealed, and Ag-decorated nanotube samples. The N 1s peak observed at 402.3 eV can be attributed either to incorporation of nitrogen into the nanotubes [82, 83] or to chemisorbed nitrogen [82-84]. Clearly one can see a small shoulder at 400 ± 0.2 eV (Figure 4.3c ii, iii), which can be ascribed to γ-N state, which is molecularly chemisorbed N_2. Additionally, the peak at 396 ± 0.2 eV belongs to β-N state, which is essentially atomic N in the form of mixed titanium oxide-nitride ($TiO_{2-x}N_x$). This indicates that the heat treatment in ammonia atmosphere indeed leads to the substitution of some oxygen sites by nitrogen [84], see Table 4.2. This finding is in good agreement with previous results on N-doped TiO_2 [49]. Figure 4.3d is Ag 3d core level XPS scan over a small energy window at higher resolution. The Ag $3d_{5/2}$ peak appears at 368.3 eV and the Ag $3d_{3/2}$ peak is found at 374.3 eV, with a splitting of the 3d

doublet of 6.0 eV, indicating that Ag mainly exists in metallic state on the sample of Ag-decorated nanotubes. [85, 86]

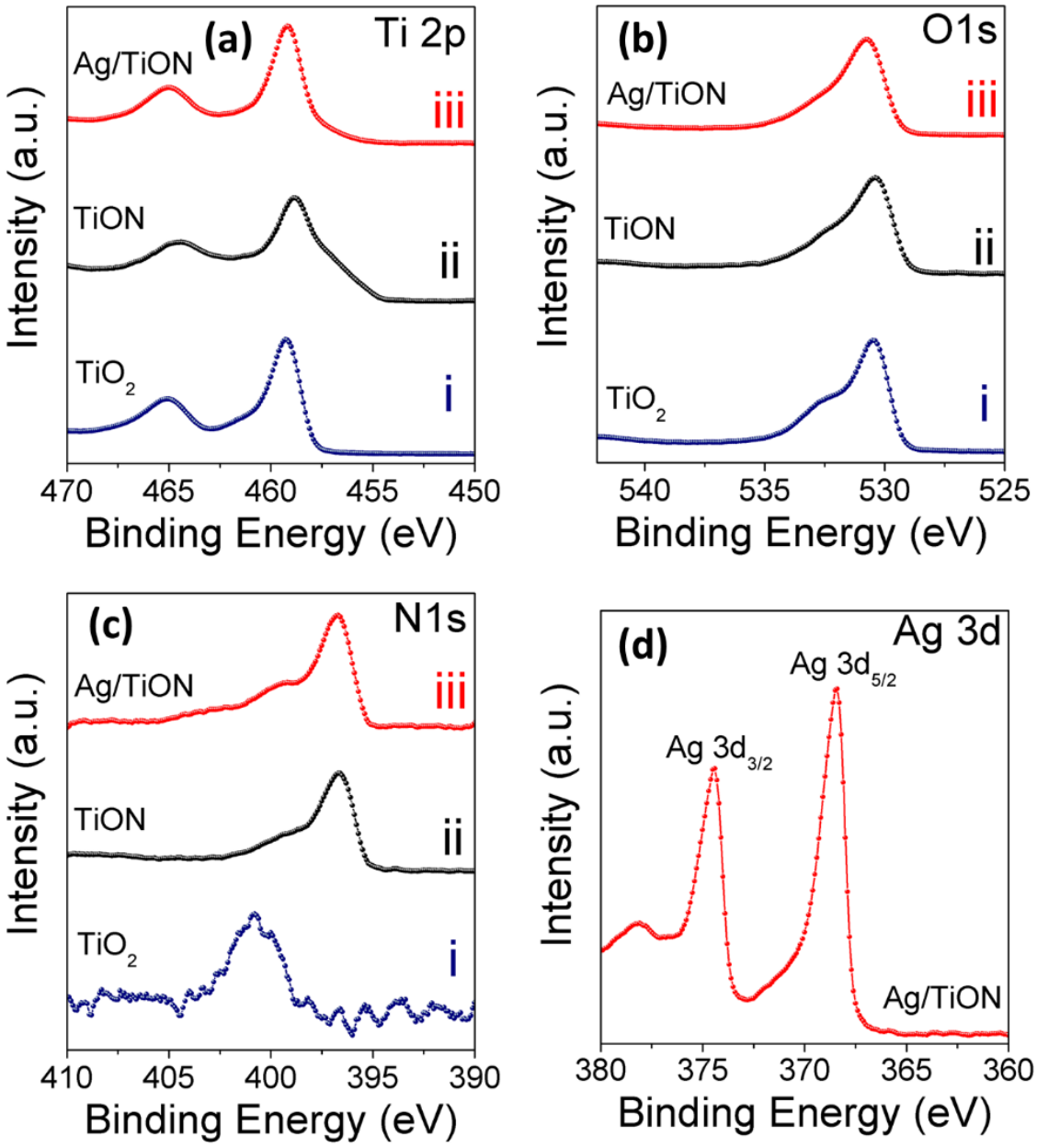

Figure 4.3 XPS spectra of the (i) air-annealed, (ii) ammonia-annealed, and (iii) Ag-decorated ammonia-annealed nanotube samples.

Table 4.1 Atomic percentage of Ti, O, N and Ag for the air-annealed, ammonia-annealed, and Ag-decorated ammonia-annealed samples as extracted from XPS.

Sample	Ti	O	N	Ag
Air-annealed	21.93	76.86	1.21	------
Ammonia-annealed	23.31	44.62	32.07	-------
Ag-decorated ammonia annealed	38.23	54.34	6.87	1.09

Table 4.2 Traditional and Kröger-Vink notations of defects in TiO_2 and N-doped TiO_2 systems

Traditional Notation	Description	Kröger-Vink Notation
Ti_{Ti}^{+4}	Ti^{+4} ion in titanium lattice site	Ti_{Ti}^{x}
Ti_{Ti}^{+3}	Ti^{+3} ion in titanium lattice site	e’
V_{Ti}	Titanium vacancy	V_{Ti}''''
Ti_i^{+3}	Ti^{+3} in an interstitial site	$Ti_i^{\bullet\bullet\bullet}$
Ti_i^{+4}	Ti^{+4} in an interstitial site	$Ti_i^{\bullet\bullet\bullet\bullet}$
O_O^{-2}	O^{-2} ion in an oxygen lattice site	O_O^{x}
V_O	Oxygen vacancy	$V_O^{\bullet\bullet}$
O_O^{-}	O^{-} ion in an oxygen lattice site	$h^{\bullet}$
N_O^{-3}	N^{-3} ion in an oxygen lattice site	N_O'''
N_i^{-3}	N^{-3} ion in an interstitial site	$N_i^{\bullet\bullet\bullet}$

Figure 4.4a, shows the UV-Vis absorption spectra of as-anodized, air-annealed and Ag/ammonia-annealed nanotube (Ag/TiON) samples. Annealing in air resulted in a small red-shift in the absorption wavelength from 385 nm (3.2eV) to 410 nm (3.03 eV). However, annealing in ammonia resulted in a significant red-shift in the visible region up to 512 nm (2.4 eV). Note also the hump at 430 nm, which could be related to the presence of Ag nanoparticles. This agrees with Ferrero *et al.* [47] who showed that titanium oxynitride mesoporous thin films are efficient visible-light-active photocatalysts due to the discrete introduction of N, which caused a shift of the titania absorption edge. The photocatalytic activity of the fabricated Ag/TiON nanotubes was investigated by using them as photoanodes to split water under AM 1.5 G one-sun illumination. Figure 4.4b shows the photocurrent density of the air-annealed, oxynitride, and Ag/oxynitride nanotube electrodes. The photocurrent produced by the air-annealed nanotube (0.15 mA/ cm^2 at 1.0 V_{SCE}) is found to be in agreement with those reported in the literature, [87] indicting the high quality of the nanotubes. Interestingly, the oxynitride nanotubes showed exceptional enhancement in the photocurrent density (6 mA/cm^2 at 1.0 V_{SCE}) compared to the air-annealed nanotubes and also compared to that reported for TiN nanostructured thin film (0.2 mA/ cm^2 at 1.0 $V_{Ag/AgCl}$) [88]. Such an enhancement is in accordance with the absorption spectra shown in Figure 4.4a. Upon addition of the Ag nanoparticles to the oxynitride nanotubes, the photocurrent significantly increased to 14 mA/cm^2 at 1.0 V_{SCE}. Such enhancement can be relatd to increasing the conductivity and the possible plasmonic effect of Ag nanoparticles. This agrees with the onset potential, the light contribution toward the minimum potential needed for water splitting process to take place, as it is shifted to more negative values in the order: TiO_2 (-0.749 V_{SCE}) < TiON (-0.84 V_{SCE}) < Ag/TiON (-0.961 V_{SCE}). Therefore, the Ag/TiON nanotubes

photoanode requires less voltage for water oxidation than the TiO_2 and TiON nanotube photoanodes counterparts, indicating more favorable photoelectrochemical activity.

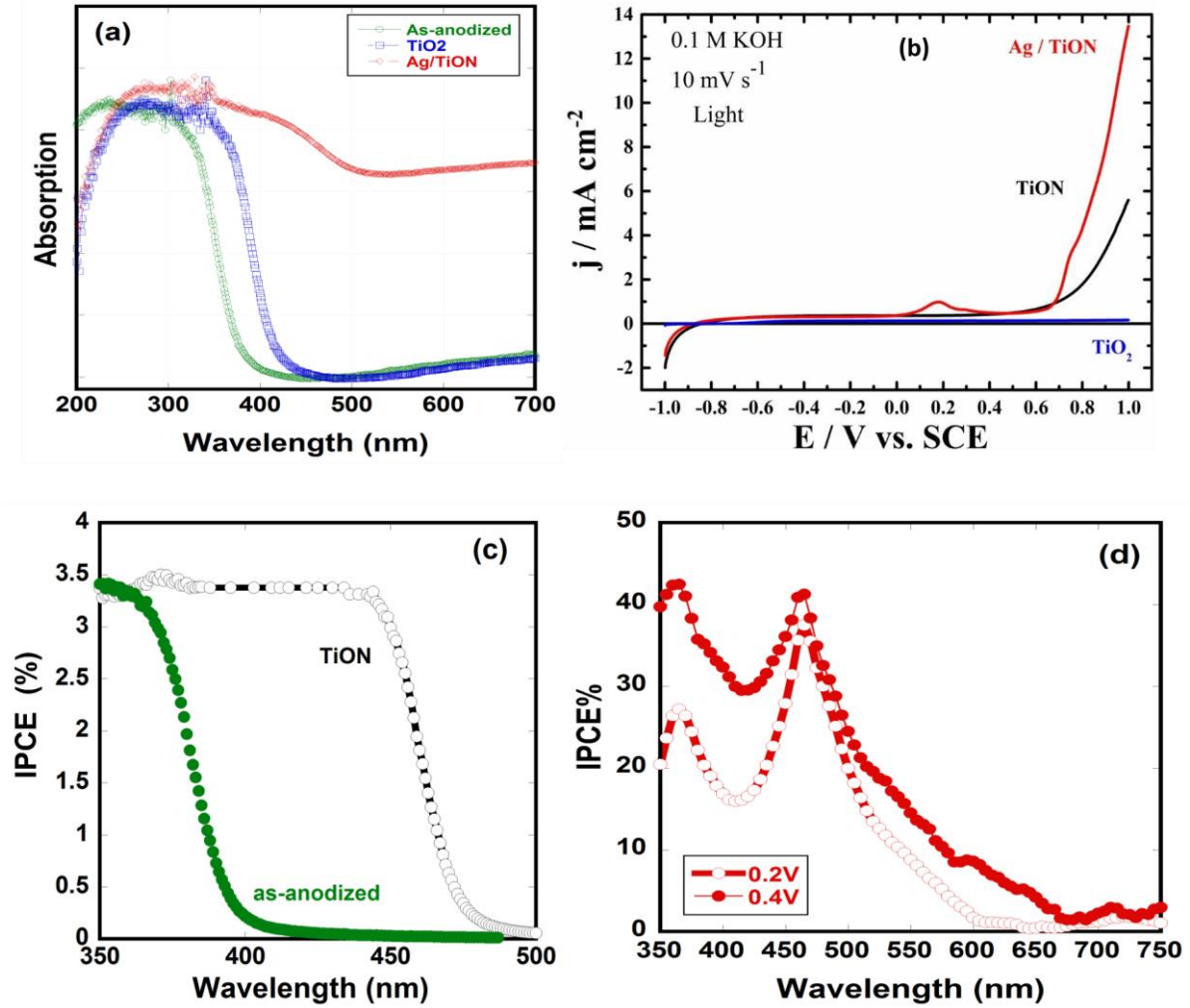

Figure 4.4 (a) UV-Vis absorption spectra of as-anodized nanotubes, TiO_2 nanotubes annealed in air and Ag-decorated TiON nanotubes(Ag/TiON), (b) linear sweep voltammetry under illumination of TiO_2, TiON and Ag/TiON, (c) the IPCE under no bias of as-anodized and TiON samples, and (d) the IPCE of Ag/TiON under applied bias.

The incident photon conversion efficiency (IPCE) experiments were performed in a two-electrode arrangement with the TiO_2, TiON, or Ag/TiON nanotube array films as the working photoelectrodes and platinum foil as a counter electrode in 0.1 M KOH solution. Figure 4.4c shows the obtained IPCE for the nanotube array films as a function of the irradiation wavelength under no bias. The IPCE was calculated using Eq 5, where λ is the wavelength of

incident light, i_{ph} is the photocurrent density under illumination at λ and I_o is the incident light intensity at λ.

$$IPCE\% = \frac{(1240\ eV.nm) \times (i_{ph}\ mA.cm^{-2})}{(\lambda\ nm) \times (I_o\ mW.cm^{-2})} \times 100 \qquad \text{Equation 4-1}$$

The obtained IPCE values, Figure 4.4c, in the wavelength range from 400 to 550 nm indicate the activity of TiON films in the visible light, in accordance with the absorption spectra shown in Figure 4.4a. Note that the Ag/TiON films showed similar IPCE behavior except for a small hump at 480 nm. The applied bias assists the separation of the photogenerated electron-hole pairs, thereby enhancing the IPCE. Upon the use of 0.2V and 0.4V (Figure 4.4Fd), Ag/TiON films showed an enhancement in the IPCE: between 350-400 nm, the IPCE increases up to 25%, then it further increases to 41% in the wavelength range 450-510 nm, after which it declines indicating that the photocurrent occurs as a result of the band gap transition. Note that the maximum IPCE peak was observed around 480 nm, which is the commonly reported plasmonic peak or Ag nanoparticles [89], suggesting that the enhancement in the photoelectrochemical activity is partially supported by the plasmonic effect of Ag NPs. The obtained IPCE for TiON and Ag/TiON nanotube films are much higher than that obtained for the pristine TiO_2 nanotube film, in good agreement with the UV-vis DRS results shown in Figure 4.4a. We note that our obtained IPCE is higher than that reported for N-doped titanium dioxide nanotube arrays [90].

Considering the correlation between the structure of the fabricated photoanodes and the observed enhanced photo response, the thin wall thickness of the synthesized TiON nanotube arrays is expected to play a vital role. The nanotubular architecture, with a wall thickness of 14±2 nm, ensures that the photogenerated holes are never generated far from the

semiconductor-electrolyte interface [1]. Furthermore, since half the wall thickness is significantly less than the minority carrier diffusion length (~20 nm in TiO_2) [91], charge-carrier separation takes place efficiently. The potential drop ($\Delta\emptyset_0$) within the tube wall was shown to follow the relation [87]:

$$\Delta\emptyset_0 = \frac{kTr_0^2}{6eL_D^2} \qquad \textit{Equation 4-2}$$

where r_0 is half the width of the wall, T is the temperature, and L_D is the Debye length, given by: [92]

$$L_D = [\frac{\varepsilon\varepsilon_0 kT}{2e^2 N_D}]^2 \qquad \textit{Equation 4-3}$$

where N_D is the number of ionized donors per cubic centimeter [92]. It is important to note that this potential drop across the wall thickness may not be enough to separate the photogenerated electrons and holes. However, because of the nanoscale dimensions of the walls, the holes can easily diffuse into the surface, which was shown to takes place on a scale of picoseconds [93]. It was also reported that minority carriers generated within a distance from the surface equal to the sum of the depletion layer width and the diffusion length (retrieval length) escape recombination and reach the electrolyte [94]. Note that the relevant dimensional features of our TiON nanotube arrays (half the wall thickness) are all smaller than 10 nm, which is the range reported for crystalline TiO_2 retrieval length [95]. Therefore, bulk recombination is expected to be reduced and the photoconversion efficiency to be enhanced [96-98].

Chapter 5: CO_2 activation on bimetallic Cu-Ni

GAXRD analysis was performed to investigate the structure of the alloys. Figure 5.1 shows the GAXRD patterns of Cu-Ni alloys. The diffraction pattern for pure Cu shows peaks characteristic for (111), (200), and (220) planes at 43.254°, 50.375°, and 73.997° respectively. Alternatively, pure Ni shows the same peaks at 44.169°, 51.462°, and 75.756° for (111), (200), and (220) planes, respectively. This data corresponds well to the ICDD cards for pure Cu (black) pure Ni (red) as labeled on Figure 5.1.

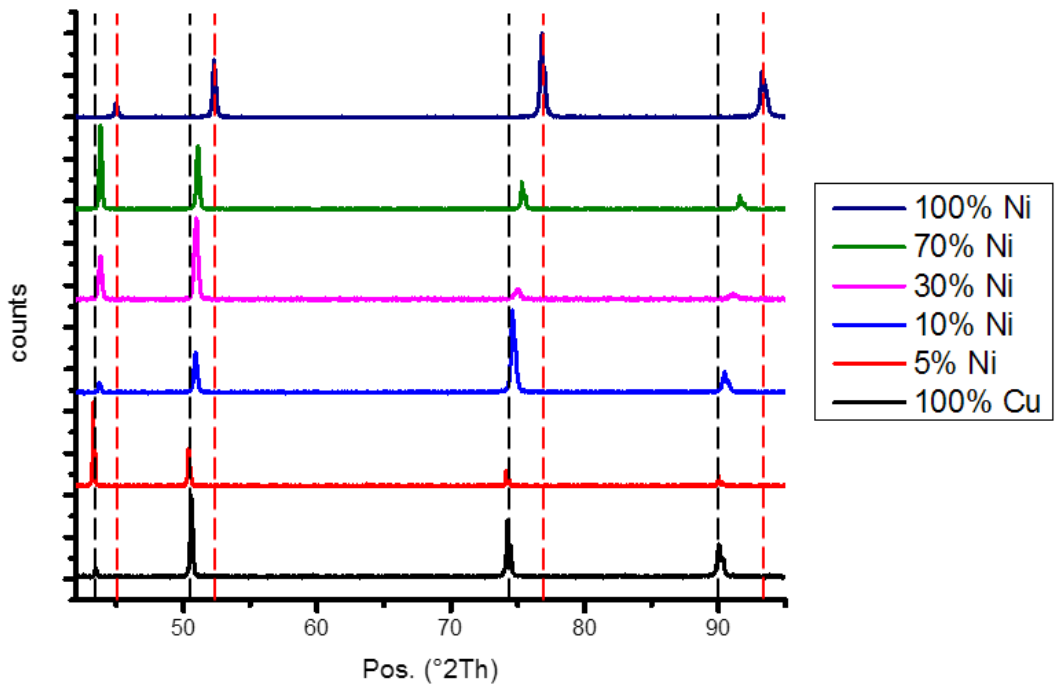

Figure 5.1 GAXRD diffraction pattern for as received alloy samples showing peaks for (a) (111) (b) (200) (c) (220) planes of fcc structure of Cu-Ni alloys.

As Ni content increases, a shift to higher diffraction angles and a shortening of the lattice parameters were observed as shown in Table 5.1. This is interesting because as Ni content increases, the bond energy of the atoms also increases, and a shortening of the bond length causes this shift [99]. The rise in bond strength is further justified by the difference in melting points, Ni at 1728 K and Cu at 1358 K.

Table 5.1 Lattice parameters and strain calculated from GAXRD data

	Lattice parameters			Strain (%)
	a	b	c	
Cu	3.6077	3.6077	3.6077	0.055701
5% Ni	3.6025	3.6025	3.6025	0.107982
10% Ni	3.5934	3.5934	3.5934	0.059717
30% Ni	3.5720	3.5720	3.5720	0.260189
70% Ni	3.5450	3.5450	3.5450	0.243464
Ni	3.5140	3.5140	3.5140	0.070471

Figure 5.2 shows the LSV sweeps for electropolished metals in CO_2-saturated 0.1M KOH, where the addition of Ni reduces the overpotential needed to drive the CO_2 reduction reaction. However, the improvement that the addition of Ni offers diminishes at Ni content >30%. This 30% threshold of Ni was shown in the work of Kitayama *et al.* where the CO formation rate was promoted by adding a small amount of Ni to Cu over SiO_2 support [100]. Chronoamperometry measurements also confirm that the addition of 30% Ni to Cu is best for improved performance. As seen in Figure 5.3, reaction kinetics are improved, and no surface inactivation is observed with a rise in current over time. The same is not observed for pure Copper due to poor kinetics and surface poisoning, a common problem of Cu electrodes [101].

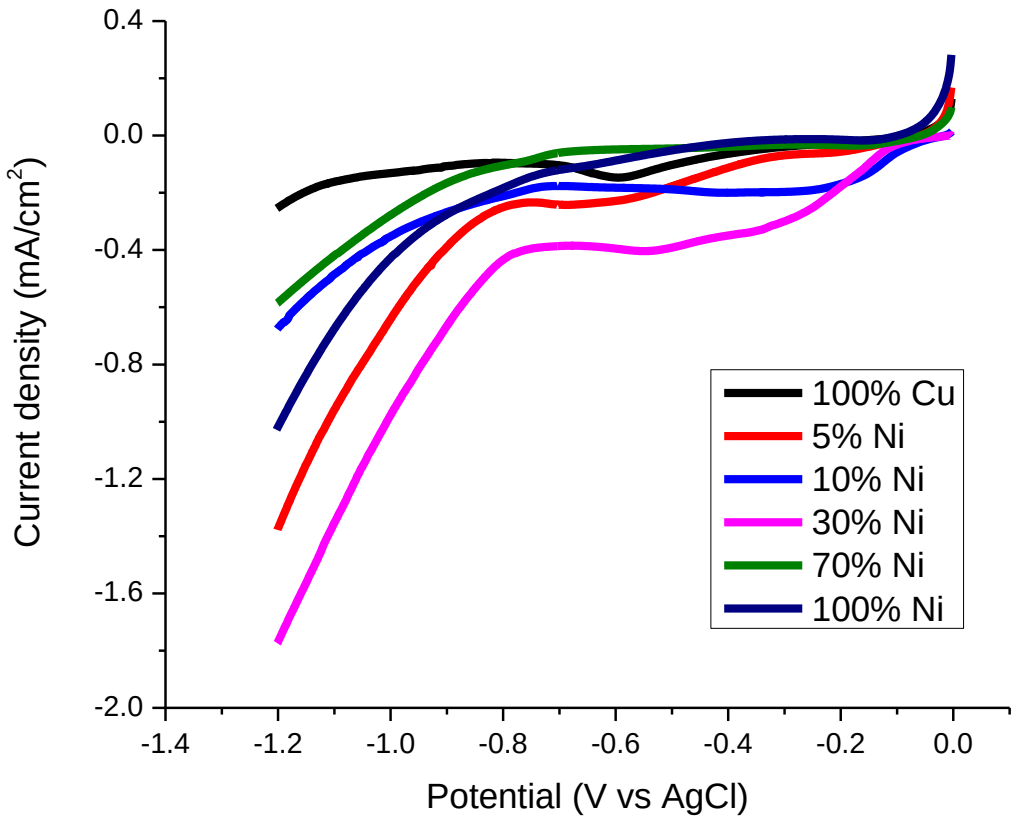

In increasing order	Nickel content (%)	Overpotential (vs sat' AgCl)	Current density (mA/cm²)
	30	**-0.7 V**	**-1.8**
	5	-0.8 V	-1.4
	10	-0.8 V	-0.7
	100	-0.9 V	-1.0
	70	-0.9 V	-0.6
	0	-1.0 V	-0.3

Figure 5.2 LSV in CO_2 saturated 0.1M KOH at a scan rate of 0.2V-s^{-1}

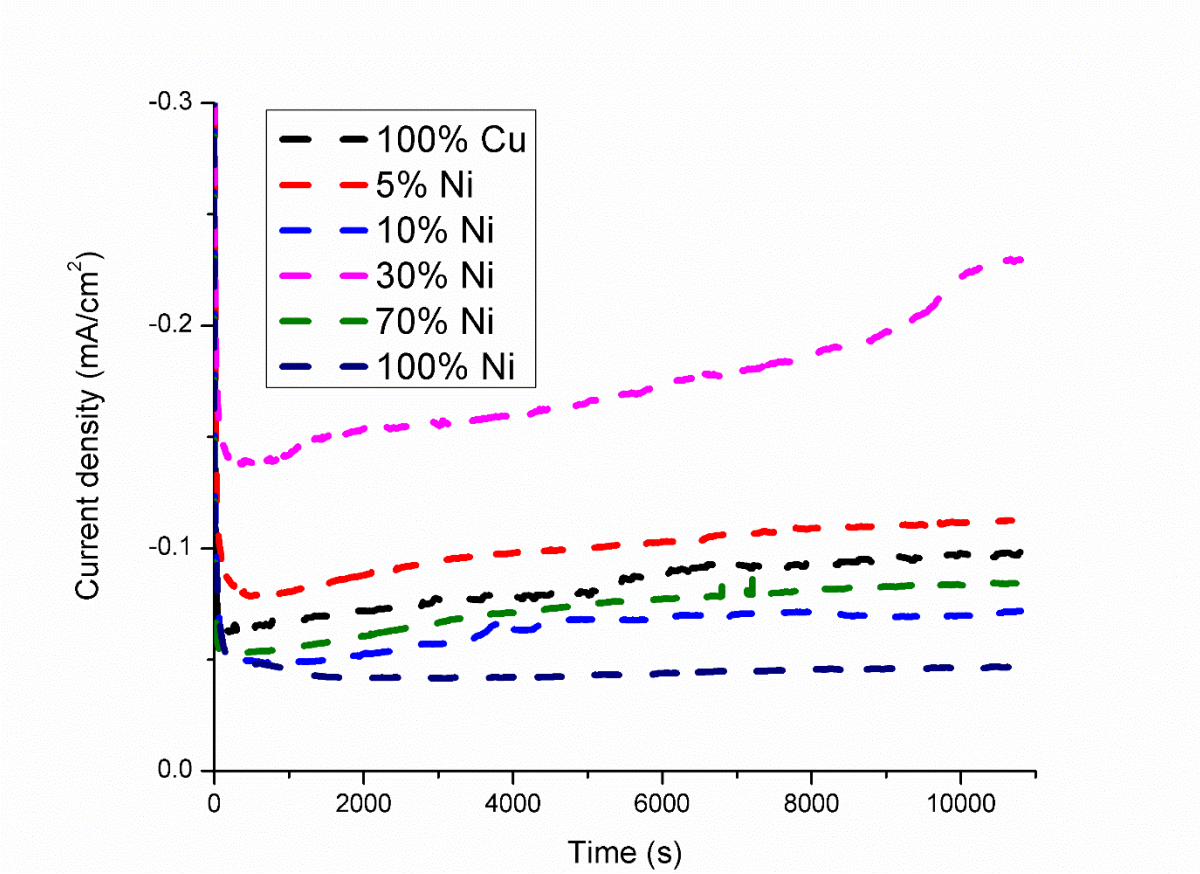

Figure 5.3 Chronoamperometery mearsurements at 0.5V(NHE vs AgCl)

These findings can be explained by changes in the surface interaction and charge transfer behavior of CO_2 at the 30% Ni electrode. Preliminary computational calculations for the predominant (111) planes of the alloy reveal that adding Ni leads to a higher CO_2 adsorption energy on the surface. The nature of this adsorption is chemisorption as opposed to only physisorption on pure copper electrodes. In Figure 5.4a, the adsorption on Cu only marginal perturbated the CO_2 molecule and the linear O-C-O angle remained nearly 180°. Thus, the CO molecule is not activated, and the adsorption is a physisorption process. The weak Cu-C bond is evidenced by the relatively large Cu-C bond length of 2.5 A. On the other hand, Figure 5.4b shows that the adsorption on Ni resulted in an evidenced perturbation of the CO_2 molecule, where the linear O-C-O angle changed from 180° to 133.8°, thereby activating it. The adsorption process over Ni surface is a chemisorption. Ni atoms interacted with the CO_2

molecule from the C end (because it's more electronegative) with a shorter Ni-C bond length of 1.95 A. In this case, the CO_2 molecule is more strongly attached to the Ni surface atoms compared to the adsorption on Cu.

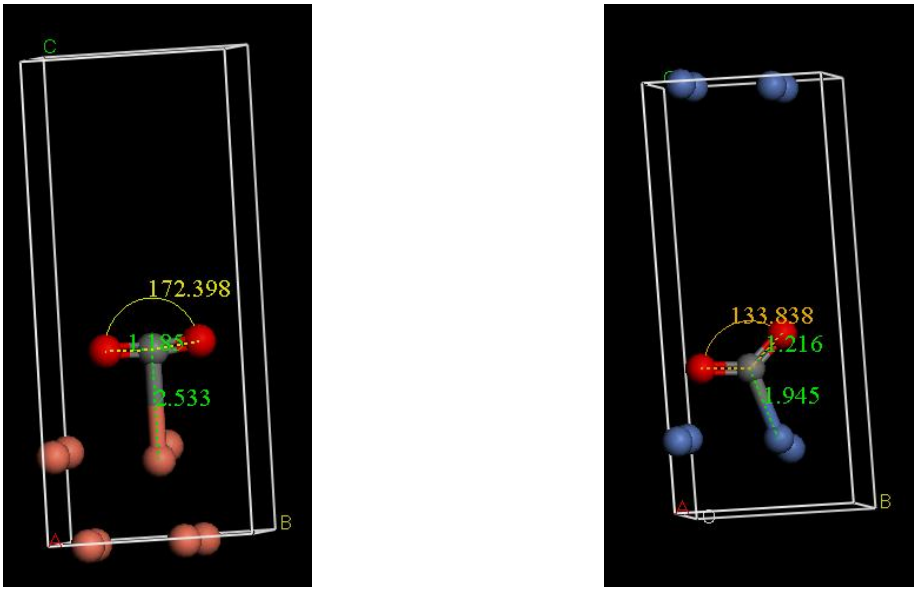

Figure 5.4 DFT results for the adsorption of CO_2 on Cu (red) and Ni (blue)

However, in Figure 5.3 significantly better charge transfer to the CO_2 molecules is only observed for 30% Ni, suggesting that other factors are at play and a threshold value of 30% is warranted. GAXRD data revealed a dependence of Ni content and lattice strain. Lattice strain initially drops then reaches a maximum at 30% Ni, higher than Cu, as shown in Table 5.1. It is well-established in the work of Hongwen *et al.* that the upward shift of d-band center pushes more of the antibonding states above the Fermi level, resulting in the decreasing occupation and stronger adsorbate bonding [102]. Accordingly, we can conclude that the tensile strain on the surface of 30% Ni shifts up the d-band center of surface atoms, thereby strengthening the adsorption of CO_2. Additionally, the improved binding is also due to surface atoms now having a higher coordination number and more dangling bonds, allowing better surface interactions. With better surface interactions, bending of the C-O bonds leads to better molecule activation.

Chapter 6: Conclusion and Future Work

In this research we investigated the generation of solar fuels: H_2 and CH_4, through solar water splitting and electrochemical reduction of CO_2.

From the work presented in Chapter 44, we investigated the fabrication of TiO_2 nanotubes and its decoration with Ag nanoparticles for water splitting applications. The following conclusions are drawn:

1. The as-anodized TiO_2 array films retain their morphology upon annealing in ammonia atmosphere, realizing the opportunity to convert TiO_2 into TiON at temperatures as low as 600 $^{\circ}$C.
2. Titanium oxynitride nanotubes showed significant increase in the photocurrent (6 mA/cm^2) compared to the as-anodized TiO_2 nanotubes counterpart (0.15 mA/cm^2).
3. Decorating the TiON nanotubes with Ag nanoparticles resulted in exceptionally high photocurrent reaching 14 mA/cm^2 at 1.0 V_{SCE}.
4. This enhancement in the photocurrent is related to the synergistic effects of Ag decoration, nitrogen doping, and the unique structural properties of the fabricated nanotube arrays.
5. This proposed platform of titanium oxynitride nanotubes array films holds promise for a variety of applications of the future design of optoelectronic devices.

From the work presented in Chapter 5, we investigated the enhancement in electrochemical CO_2 reduction of adding Ni to Cu. The following conclusions are drawn:

1. The effect of loading 5%, 10%, 30% and 70% Ni in Cu was investigated.

2. Characterization of the as-receive alloys was performed using GAXRD. Micro strain values revealed a unique strain value for adding 30% Ni to Cu. The observed strain value of 0.260% was significantly higher than pure Cu (0.056%) and pure Ni (0.070%), respectively.
3. Overpotential values for the electrochemical reduction of CO_2 was lowest for 30% Ni -0.7V vs AgCl, with a peak current density of -1.8mA/cm^2. Long duration, low voltage (-0.5V NHE) chronoamperometry measurements revealed that 30% Ni is superior. No limiting current was observed for 3 hours, which indicated no surface poisoning.
4. DFT calculations were used to validate the CO_2 adsorption type on the surface. It was concluded that Cu atoms only offer physisorption to CO_2 molecules while for Ni atoms the interaction in chemisorption. This explains the general improvement Ni offers to Cu.
5. Lattice strain values for all samples revealed a volcano plot with a peak strain at 30% Ni. An increase in tensile strain boosts the catalytic activity by shifting up the d-band center and thus strengthening the adsorption of key intermediates. This explains why the addition of 30% Ni results in the least overpotential for the electrochemical reduction of CO_2.

Finally, here are some points that are suggested for future work:

1. Decorating TNTS with bimetallic nanoparticles for the photoelectrochemical reduction of CO_2.
2. It has been documented that metal oxides (namely copper oxide) has superior properties to metallic copper. To the best of my knowledge the properties of bimetallic alloys such as Cu-Ni oxides are still unresearched.

References

1. Grimes, C., Varghese, O. & Ranjan, S. *Light, water, hydrogen: the solar generation of hydrogen by water photoelectrolysis* (Springer, US, 2008).

2. Shafiee, S. & Topal, E. When will fossil fuel reserves be diminished? *Energy Policy* **37,** 181-189 (2009).

3. Panwar, N. L., Kaushik, S. C. & Kothari, S. Role of renewable energy sources in environmental protection: a review. *Renewable and Sustainable Energy Reviews* **15,** 1513-1524 (2011).

4. United States Environmental Protection Agency Greenhouse Gas Inventory Data Explorer: US EPA. https://www3.epa.gov/climatechange/ghgemissions/inventoryexplorer/index.html#iallsectors/carbondioxide/inventsect/current (accessed Feb 7, 2018).

5. Edwards, P. P., Kuznetsov, V. L., David, W. I. & Brandon, N. P. Hydrogen and fuel cells: towards a sustainable energy future. *Energy Policy* **36,** 4356-4362 (2008).

6. Hsiung, S. Hydrogen fuel cell engines and related technologies. (2001).

7. Midilli, A., Ay, M., Dincer, I. & Rosen, M. A. On hydrogen and hydrogen energy strategies: I: current status and needs. *Renewable and sustainable energy reviews* **9,** 255-271 (2005).

8. Gupta, R. B. *Hydrogen fuel: production, transport, and storage* (CRC Press, Boca Raton, 2009).

9. de Krol, R. v. & Grätzel, M. *Photoelectrochemical hydrogen production* (Springer, New York, 2012).

10. Green, Alex, E. S., Schaefer & Greg, P. *What to do with CO_2* (American Chemical Society, 2001).

11. Usubharatana, P., McMartin, D., Veawab, A. & Tontiwachwuthikul, P. Photocatalytic process for CO_2 emission reduction from industrial flue gas streams. *Ind Eng Chem Res* **45,** 2558-2568 (2006).

12. Fujishima, I. & Honda, K. Photoelectrolysis of water using titanium oxide. *Nature* **238,** 38 (1972).

13. Scibioh, M. A. & Viswanathan, B. Hydrogen Future: Facts and Fallacies. *Bulletin of the catalysis Society of India* **3,** 72-81 (2004).

14. White, J. L., et al. Light-driven heterogeneous reduction of carbon dioxide: photocatalysts and photoelectrodes. *Chem.Rev.* **115,** 12888-12935 (2015).

15. Qiao, J., Liu, Y. & Zhang, J. *Electrochemical Reduction of Carbon Dioxide: Fundamentals and Technologies* (CRC Press, 2016).

16. Diebold, U. Structure and properties of TiO_2 surfaces: a brief review. *Applied physics A* **76,** 681-687 (2003).

17. Mo, S. & Ching, W. Y. Electronic and optical properties of three phases of titanium dioxide: Rutile, anatase, and brookite. *Physical Review B* **51,** 13023 (1995).

18. Palmisano, L. & Sclafani, A. Thermodynamics and kinetics for heterogeneous photocatalytic processes. *Heterogeneous photocatalysis* **3,** 110 (1997).

19. Demeestere, K., Dewulf, J. & Van Langenhove, H. Heterogeneous photocatalysis as an advanced oxidation process for the abatement of chlorinated, monocyclic aromatic and sulfurous volatile organic compounds in air: state of the art. *Crit.Rev.Environ.Sci.Technol.* **37,** 489-538 (2007).

20. Kočí, K., Obalová, L. & Lacný, Z. Photocatalytic reduction of CO_2 over TiO_2 based catalysts. *Chemical Papers* **62,** 1-9 (2008).

21. Stroyuk, A. L., Kryukov, A. I., Kuchmii, S. Y. & Pokhodenko, V. D. Semiconductor photocatalytic systems for the production of hydrogen by the action of visible light. *Theoretical and Experimental Chemistry* **45,** 209 (2009).

22. Jeyalakshmi, V., Rajalakshmi, K., Mahalakshmy, R., Krishnamurthy, K. R. & Viswanathan, B. Application of photo catalysis for mitigation of carbon dioxide. *Research on Chemical Intermediates* **39,** 2565-2602 (2013).

23. Rajeshwar, K. Fundamentals of semiconductor electrochemistry and photoelectrochemistry. *Encyclopedia of electrochemistry* (2007).

24. Varghese, O. K., Paulose, M., LaTempa, T. J. & Grimes, C. A. High-Rate Solar Photocatalytic Conversion of CO_2 and Water Vapor to Hydrocarbon Fuels. *Nano Letters* **9,** 731-737 (2009).

25. Tseng, I., Chang, W. & Wu, J. C. Photoreduction of CO_2 using sol–gel derived titania and titania-supported copper catalysts. *Applied Catalysis B: Environmental* **37,** 37-48 (2002).

26. Hoyer, P. Formation of a Titanium Dioxide Nanotube Array. *Langmuir* **12,** 1411-1413 (1996).

27. Roy, P., Berger, S. & Schmuki, P. TiO_2 nanotubes: synthesis and applications. *Angewandte Chemie International Edition* **50,** 2904-2939 (2011).

28. Macak, J. M., et al. TiO_2 nanotubes: Self-organized electrochemical formation, properties and applications. *Current Opinion in Solid State and Materials Science* **11,** 3-18 (2007).

29. Zwilling, V., et al. Structure and physicochemistry of anodic oxide films on titanium and TA6V alloy. *Surf.Interface Anal.* **27,** 629-637 (1999).

30. Macak, J. M., Sirotna, K. & Schmuki, P. Self-organized porous titanium oxide prepared in Na2SO4/NaF electrolytes. *Electrochimica Acta* **50,** 3679-3684 (2005).

31. Albu, S. P., Ghicov, A., Macak, J. M. & Schmuki, P. 250 µm long anodic TiO_2 nanotubes with hexagonal self-ordering. *physica status solidi (RRL)-Rapid Research Letters* **1,** (2007).

32. Paulose, M., et al. Anodic growth of highly ordered TiO_2 nanotube arrays to 134 microm in length. *The journal of physical chemistry. B* **110,** 16179 (2006).

33. Tsuchiya, H., et al. Self-organized TiO_2 nanotubes prepared in ammonium fluoride containing acetic acid electrolytes. *Electrochemistry communications* **7,** 576-580 (2005).

34. MACAK, J. & SCHMUKI, P. Anodic growth of self-organized anodic TiO_2 nanotubes in viscous electrolytes. *Electrochimica Acta* **52,** 1258-1264 (2006).

35. Mor, G. K., Varghese, O. K., Paulose, M., Shankar, K. & Grimes, C. A. A review on highly ordered, vertically oriented TiO_2 nanotube arrays: Fabrication, material properties, and solar energy applications. *Solar Energy Materials and Solar Cells* **90,** 2011-2075 (2006).

36. Watcharenwong, A., et al. Self-organized TiO_2 nanotube arrays by anodization of Ti substrate: effect of anodization time, voltage and medium composition on oxide morphology and photoelectrochemical response. *J.Mater.Res.* **22,** 3186-3195 (2007).

37. Gong, D., et al. Titanium oxide nanotube arrays prepared by anodic oxidation. *J.Mater.Res.* **16,** 3331-3334 (2001).

38. Fierro, J. L. G. *Metal oxides: chemistry and applications* (CRC press, 2005).

39. Sakthivel, S., et al. Enhancement of photocatalytic activity by metal deposition: characterisation and photonic efficiency of Pt, Au and Pd deposited on TiO_2 catalyst. *Water Res.* **38,** 3001-3008 (2004).

40. Habisreutinger, S. N., Schmidt-Mende, L. & Stolarczyk, J. K. Photocatalytic reduction of CO_2 on TiO_2 and other semiconductors. *Angewandte Chemie International Edition* **52,** 7372-7408 (2013).

41. Hitoki, G., et al. (Oxy)nitrides as new photocatalysts for water splitting under visible light irradiation. *Electrochemistry* **70,** 463-465 (2002).

42. Allam, N. K., Poncheri, A. J. & El-Sayed, M. A. Vertically Oriented Ti-Pd Mixed Oxynitride Nanotube Arrays for Enhanced Photoelectrochemical Water Splitting. *Acs Nano* **5,** 5056-5066 (2011).

43. Fuertes, A. Chemistry and applications of oxynitride perovskites. *Journal of Materials Chemistry* **22,** 3293-3299 (2012).

44. Allam, N. K., Shaheen, B. S. & Hafez, A. M. Layered Tantalum Oxynitride Nanorod Array Carpets for Efficient Photoelectrochemical Conversion of Solar Energy: Experimental and DFT Insights. *Acs Applied Materials & Interfaces* **6,** 4609-4615 (2014).

45. Chen, X. B. & Burda, C. Photoelectron spectroscopic investigation of nitrogen-doped titania nanoparticles. *J Phys Chem B* **108,** 15446-15449 (2004).

46. Vitiello, R. P., et al. N-Doping of anodic TiO_2 nanotubes using heat treatment in ammonia. *Electrochemistry Communications* **8,** 544-548 (2006).

47. Martinez-Ferrero, E., et al. Nanostructured titanium oxynitride porous thin films as efficient visible-active photocatalysts. *Advanced Functional Materials* **17,** 3348-3354 (2007).

48. Kim, D., Fujimoto, S., Schmuki, P. & Tsuchiya, H. Nitrogen doped anodic TiO_2 nanotubes grown from nitrogen-containing Ti alloys. *Electrochemistry Communications* **10,** 910-913 (2008).

49. Asahi, R., Morikawa, T., Ohwaki, T., Aoki, K. & Taga, Y. Visible-light photocatalysis in nitrogen-doped titanium oxides. *Science* **293,** 269-271 (2001).

50. Gebauer, C., et al. Novel N, C doped Ti(IV)-oxides as Pt-free catalysts for the O-2 reduction reaction. *Electrochim.Acta* **146,** 335-345 (2014).

51. Youngblood, W. J., Lee, S. A., Maeda, K. & Mallouk, T. E. Visible Light Water Splitting Using Dye-Sensitized Oxide Semiconductors. *Acc.Chem.Res.* **42,** 1966-1973 (2009).

52. Wang, L., et al. A dye-sensitized visible light photocatalyst-Bi24O31Cl10. *Scientific Reports* **4,** 7384 (2014).

53. Roy, P., Kim, D., Lee, K., Spiecker, E. & Schmuki, P. TiO_2 nanotubes and their application in dye-sensitized solar cells. *Nanoscale* **2,** 45-59 (2010).

54. Tsuchiya, H., et al. TiO_2 nanotube layers with metallic nanoparticles. **165,** 012037 (2009).

55. Paramasivalm, I., Macak, J. M. & Schmuki, P. Photocatalytic activity of TiO_2-nanotube layers loaded with Ag and Au nanoparticles. *Electrochemistry Communications* **10,** 71-75 (2008).

56. Paramasivam, I., Macak, J. M., Ghicov, A. & Schmuki, P. Enhanced photochromism of Ag loaded self-organized TiO_2 nanotube layers. *Chemical Physics Letters* **445,** 233-237 (2007).

57. Seery, M. K., George, R., Floris, P. & Pillai, S. C. Silver doped titanium dioxide nanomaterials for enhanced visible light photocatalysis. *Journal of Photochemistry and Photobiology A-Chemistry* **189,** 258-263 (2007).

58. Arabatzis, I. M., et al. Silver-modified titanium dioxide thin films for efficient photodegradation of methyl orange. *Applied Catalysis B-Environmental* **42,** 187-201 (2003).

59. Inoue, T., Fujishima, A., Konishi, S. & Honda, K. Photoelectrocatalytic reduction of carbon dioxide in aqueous suspensions of semiconductor powders. *Nature* **277,** 637-638 (1979).

60. Halmann, M., Ulman, M. & Aurian-Blajeni, B. Photochemical solar collector for the photoassisted reduction of aqueous carbon dioxide. *Solar Energy* **31,** 429-431 (1983).

61. Halmann, M., Katzir, V., Borgarello, E. & Kiwi, J. Photoassisted carbon dioxide reduction on aqueous suspensions of titanium dioxide. *Solar Energy Materials* **10,** 85-91 (1984).

62. Jin, L. *Dynamics of semiconducting nanocrystals uptake into mesoporous TiO_2 thick films through electrophoretic deposition and its application in solar energy*, 2015).

63. Anpo, M., Yamashita, H., Ichihashi, Y. & Ehara, S. Photocatalytic reduction of CO_2 with H2O on various titanium oxide catalysts. *J Electroanal Chem* **396,** 21-26 (1995).

64. Anpo, M. & Chiba, K. Photocatalytic reduction of CO_2 on anchored titanium oxide catalysts. *Journal of Molecular Catalysis* **74,** 207-212 (1992).

65. Kuhl, K. P., Cave, E. R., Abram, D. N. & Jaramillo, T. F. New insights into the electrochemical reduction of carbon dioxide on metallic copper surfaces. *Energy & Environmental Science* **5,** 7050-7059 (2012).

66. Watanabe, M., Shibata, M., Kato, A., Azuma, M. & Sakata, T. Design of Alloy Electrocatalysts for CO 2 Reduction III. The Selective and Reversible Reduction of on Cu Alloy Electrodes. *J.Electrochem.Soc.* **138,** 3382-3389 (1991).

67. Hori, Y., Wakebe, H., Tsukamoto, T. & Koga, O. Electrocatalytic process of CO selectivity in electrochemical reduction of CO_2 at metal electrodes in aqueous media. *Electrochim.Acta* **39,** 1833-1839 (1994).

68. Adachi, K., Ohta, K. & Mizuno, T. Photocatalytic reduction of carbon dioxide to hydrocarbon using copper-loaded titanium dioxide. *Solar Energy* **53,** 187-190 (1994).

69. Chen, H., Wang, C., Yu, C., Tseng, L. & Liao, P. Carbon dioxide reforming of methane reaction catalyzed by stable nickel copper catalysts. *Catalysis Today* **97,** 173-180 (2004).

70. Jeyalakshmi, V., Mahalakshmy, R., Kr, K. & Viswanathan, B. *Photocatalytic Reduction of Carbon Dioxide by Water: A Step towards Sustainable Fuels and Chemicals*, 2012).

71. Luth, H. *Solid surfaces, interfaces and thin films* (Springer, 2001).

72. Nasution, H. W., Purnama, E., Kosela, S. & Gunlazuardi, J. Photocatalytic reduction of CO_2 on copper-doped Titania catalysts prepared by improved-impregnation method. *Catalysis Communications* **6,** 313-319 (2005).

73. Ma, S., et al. Electroreduction of Carbon Dioxide to Hydrocarbons Using Bimetallic Cu–Pd Catalysts with Different Mixing Patterns. *J.Am.Chem.Soc.* **139,** 47-50 (2017).

74. Hori, Y., Murata, A. & Takahashi, R. Formation of hydrocarbons in the electrochemical reduction of carbon dioxide at a copper electrode in aqueous solution. *Journal of the Chemical Society, Faraday Transactions 1: Physical Chemistry in Condensed Phases* **85,** 239-2326 (1989).

75. Pridmore, N. E. Nickel Based Nanoalloys as Reduction Electrocatalysts for Solar Fuel Production. *Nickel based nanoalloys as reduction electrocatalysts for solar fuel production* (2015).

76. Zielińska-Jurek, A. Progress, challenge, and perspective of bimetallic TiO 2-based photocatalysts. *Journal of Nanomaterials* **2014,** 3 (2014).

77. Qiao, J., Liu, Y., Hong, F. & Zhang, J. A review of catalysts for the electroreduction of carbon dioxide to produce low-carbon fuels. *Chem.Soc.Rev.* **43,** 631-675 (2014).

78. Luo, D., Bi, Y., Kan, W., Zhang, N. & Hong, S. Copper and cerium co-doped titanium dioxide on catalytic photo reduction of carbon dioxide with water: Experimental and theoretical studies. *J.Mol.Struct.* **994,** 325-331 (2011).

79. Zukalova, M., et al. Facile Conversion of Electrospun TiO_2 into Titanium Nitride/Oxynitride Fibers. *Chemistry of Materials* **22,** 4045-4055 (2010).

80. Lozano, M. P. & Fraxedas, J. XPS analysis of the activation process in non-evaporable getter thin films. *Surf.Interface Anal.* **30,** 623-627 (2000).

81. Zhang, F., Wolf, G. K., Wang, X. H. & Liu, X. H. Surface properties of silver doped titanium oxide films. *Surf.Coat.Technol.* **148,** 65-70 (2001).

82. Braic, M., et al. Preparation and characterization of titanium oxy-nitride thin films. *Appl.Surf.Sci.* **253,** 8210-8214 (2007).

83. Deng, Y., Tripkovic, V., Rossmeisl, J. & Arenz, M. Oxygen Reduction Reaction on Pt Overlayers Deposited onto a Gold Film: Ligand, Strain, and Ensemble Effect. *Acs Catalysis* **6,** 671-676 (2016).

84. Saha, N. C. & Tompkins, H. G. Titanium Nitride Oxidation Chemistry - an X-Ray Photoelectron-Spectroscopy Study. *J.Appl.Phys.* **72,** 3072-3079 (1992).

85. Xie, K., et al. Photoelectrocatalytic properties of Ag nanoparticles loaded TiO_2 nanotube arrays prepared by pulse current deposition. *Electrochim.Acta* **55,** 7211-7218 (2010).

86. Liang, Y. Q., Cui, Z. D., Zhu, S. L., Liu, Y. & Yang, X. J. Silver nanoparticles supported on TiO_2 nanotubes as active catalysts for ethanol oxidation. *Journal of Catalysis* **278,** 276-287 (2011).

87. Grimes, C. A. & Mor, G. K. *TiO_2 Nanotube Arrays - Synthesis, Properties, and Applications*, 2009).

88. Smith, W., et al. Visible Light Water Splitting via Oxidized TiN Thin Films. *Journal of Physical Chemistry C* **116,** 15855-15866 (2012).

89. Tanabe, I., et al. Photocatalytic growth and plasmon resonance-assisted photoelectrochemical toppling of upright Ag nanoplates on a nanoparticulate TiO_2 film. *Chemical Communications* 3621-3623 (2009).

90. Kim, H., Monllor-Satoca, D., Kim, W. & Choi, W. N-doped TiO_2 nanotubes coated with a thin TaOxNy layer for photoelectrochemical water splitting: dual bulk and surface modification of photoanodes. *Energy & Environmental Science* **8,** 247-257 (2015).

91. Butterfield, I. M., et al. Applied studies on immobilized titanium dioxide films as catalysts for the photoelectrochemical detoxification of water. *J.Appl.Electrochem.* **27,** 385-395 (1997).

92. Hagfeldt, A. & Gratzel, M. Light-Induced Redox Reactions in Nanocrystalline Systems. *Chem.Rev.* **95,** 49-68 (1995).

93. Vanmaekelbergh, D. & de Jongh, P. E. Driving force for electron transport in porous nanostructured photoelectrodes. *J Phys Chem B* **103,** 747-750 (1999).

94. Sukamto, J. P. H., Mcmillan, C. S. & Smyrl, W. Photoelectrochemical Investigations of Thin Metal-Oxide Films – TiO_2, Al_2O_3, and HfO_2 on the Parent Metals. *Electrochim.Acta* **38,** 15-27 (1993).

95. Sukamto, J. P. H., Smyrl, W. H., Mcmillan, C. S. & Kozlowski, M. R. Photoelectrochemical Measurements of Thin Oxide-Films - Multiple Internal-Reflection Effects. *J.Electrochem.Soc.* **139,** 1033-1043 (1992).

96. Benkstein, K. D., Kopidakis, N., van de Lagemaat, J. & Frank, A. J. Influence of the percolation network geometry on electron transport in dye-sensitized titanium dioxide solar cells. *J Phys Chem B* **107,** 7759-7767 (2003).

97. El-Sayed, A., et al. Defect states determined the performance of dopant-free anatase nanocrystals in solar fuel cells. *Solar Energy* **144,** 445-452 (2017).

98. Mohamed, A. M., Amer, A. W., AlQaradawi, S. Y. & Allam, N. K. On the nature of defect states in tungstate nanoflake arrays as promising photoanodes in solar fuel cells. *Physical Chemistry Chemical Physics* **18,** 22217-22223 (2016).

99. Austin, N., Butina, B. & Mpourmpakis, G. CO_2 activation on bimetallic CuNi nanoparticles. *Progress in Natural Science: Materials International* **26,** 487-492 (2016).

100. Kitayama, Y., Watanabe, Y., Muramatsu, K. & Kodama, T. Catalytic reduction of carbon dioxide on Ni-Cu alloys. *Energy* **22,** 177-182 (1997).

101. DeWulf, D. W., Jin, T. & Bard, A. J. Electrochemical and surface studies of carbon dioxide reduction to methane and ethylene at copper electrodes in aqueous solutions. *J.Electrochem.Soc.* **136,** 1686-1691 (1989).

102. Huang, H., et al. Understanding of Strain Effects in the Electrochemical Reduction of CO_2: Using Pd Nanostructures as an Ideal Platform. *Angewandte Chemie* **129,** 3648-3652 (2017).